

Volume 1 Year 2021

# ADVANCED ENGINEERING SCIENCE



## ADVANCED ENGINEERING SCIENCE

### **Aim and scope**

**Advanced Engineering Science (ADES)** is a multidisciplinary journal and covers all fields of basic science and engineering. The Journal is involved in both experimental and theoretical studies on the subject area of basic science and engineering. The Journal is a multidisciplinary journal and covers all fields of basic science and engineering. It is the main purpose of the Journal that to convey the latest development on science and technology towards the related scientists and to the readers. The Journal is also involved in both experimental and theoretical studies on the subject area of basic science and engineering. ADES is a fully free journal, which does not take any article processing charge from authors.

**Advanced Engineering Science (ADES)** is a multidisciplinary journal and covers all fields of basic science and engineering

- Aerospace Engineering
- Environmental Engineering
- Civil Engineering
- Geomatics Engineering
- Mechanical Engineering
- Geology Science and Engineering
- Mining Engineering
- Chemical Engineering
- Metallurgical and Materials Engineering
- Electrical and Electronics Engineering
- Mathematical Applications in Engineering
- Computer Engineering
- Food Engineering

## **Editor**

Prof. Dr. Murat Yakar

Mersin University, Department of Geomatics Engineering ([myakar@mersin.edu.tr](mailto:myakar@mersin.edu.tr))

## **Advisory Board**

*Prof. Dr. Mehmet Cihan AYDIN, BITLIS EREN UNIVERSITY ([mcaaydin@beu.edu.tr](mailto:mcaaydin@beu.edu.tr))*

*Associate Professor Ercan IŞIK, BITLIS EREN UNIVERSITY ([eisik@beu.edu.tr](mailto:eisik@beu.edu.tr))*

*Associate Professor Ümit BUDAK, BITLIS EREN UNIVERSITY ([ubudak@beu.edu.tr](mailto:ubudak@beu.edu.tr))*

*Associate Professor. Mehmet Baran, Ankara Yıldırım Beyazıt University ([mehmet.baran@ybu.edu.tr](mailto:mehmet.baran@ybu.edu.tr))*

*Associate Professor. Memduh Kara, Mersin University ([memduhkara@mersin.edu.tr](mailto:memduhkara@mersin.edu.tr))*

*Associate Professor. Cafer Erkın Koyuncu, Mersin University ([ckoyuncu@mersin.edu.tr](mailto:ckoyuncu@mersin.edu.tr))*

*Asst. Prof Atta-ur-Rahman, University of Peshawar ([atta-ur-rehman@uop.edu.pk](mailto:atta-ur-rehman@uop.edu.pk))*

*Dr. Mehmet Levent Ağırđır, Konya Technical University, Konya/ Turkey ([mلاغirdir@ktun.edu.tr](mailto:mلاغirdir@ktun.edu.tr))*

*Dr. Fazal Raziq, King Abdullah University Science and Technology, [Saudi Arabia](http://Saudi Arabia) ([fazal.raziq@kaust.edu.sa](mailto:fazal.raziq@kaust.edu.sa))*

*Abdell Aziiz Fatthii Abdell Aziiz Ellfadally, Basilicata University / Italian National Research Councils / National Authority for Remote Sensing and Space Sciences ([abdelaziz.elfadaly@narss.sci.eg](mailto:abdelaziz.elfadaly@narss.sci.eg)) / ([abdelaziz.elfadaly@imaa.cnr.it](mailto:abdelaziz.elfadaly@imaa.cnr.it))*

*Lec. Mustafa Buber, Selçuk University ([mbuber@selcuk.edu.tr](mailto:mbuber@selcuk.edu.tr))*

Technical support: Research Assistant Aydın Alptekin [aydinalptekin@mersin.edu.tr](mailto:aydinalptekin@mersin.edu.tr)

## RESEARCH ARTICLES

### Volume 1

---

The effect of a polygon route that is not stretched on the investigation of a rough incorrectly measured angle and edge Yener Türen, Hüseyin İnce, Nuri Erdem, Tuna Erol	1-12
Kinetic and structural study on CuAlMnNi shape memory alloy with a novel composition Oktay Karaduman, İskender Özkul, Canan Aksu Canbay	13-19
Influence of the effect of the ball burnishing process applied to Al 7075-T6 alloy in different nano-aluminum powder-added grease environment on surface quality Suleyman Cinar Cagan, Berat Baris Buldum	20-25
Shape memory effect characterization of a ternary CuAlNi high temperature SMA ribbons produced by melt spinning method Oktay Karaduman, İskender Özkul, Canan Aksu Canbay	26-33
Design parameters of sand filtration systems in wastewater treatment process Ece Kalay, Hasan Sarıoğlu, İskender Özkul	34-42

---



## The effect of a polygon route that is not stretched on the investigation of a rough incorrectly measured angle and edge

Yener Türen<sup>\*1</sup>, Hüseyin İnce<sup>2</sup>, Nuri Erdem<sup>3</sup>, Tuna Erol<sup>4</sup>

<sup>1</sup>Trakya University, Vocational School of Technical Sciences, Department of Architecture and City Planning, Edirne, Türkiye, [yenerturen@trakya.edu.tr](mailto:yenerturen@trakya.edu.tr)

<sup>2</sup>Hitit University, Vocational School of Technical Sciences, Department of Architecture and City Planning, Çorum, Türkiye, [huseyinince@hitit.edu.tr](mailto:huseyinince@hitit.edu.tr)

<sup>3</sup>Osmaniye Korkut Ata University, Faculty of Engineering, Department of Geomatics Engineering, Osmaniye, Türkiye, [nurierdem@osmaniye.edu.tr](mailto:nurierdem@osmaniye.edu.tr)

<sup>4</sup>Balikesir University, Rectorate Construction and Technical Directorate, Balıkesir, Türkiye, [terol@balikesir.edu.tr](mailto:terol@balikesir.edu.tr)

Cite this study: Türen, Y., İnce, H., Erdem, N., & Erol, T. (2021). The effect of a polygon route that is not stretched on the investigation of a rough incorrectly measured angle and edge. *Advanced Engineering Science*, 1, 01-12.

### Keywords

Polygon route  
Rough faulty edge  
Rough faulty angle  
Stretched shape of polygon route

### Research Article

Received: 01.05.2021

Revised: 22.06.2021

Accepted: 01.07.2021

Published: 15.08.2021



### Abstract

When a traverse net is in a tense position, the angles measured between the directions observed at the traverse points are close to 200°. If the angles measured between the directions observed at the traverse points are around 100° or 300°, this indicates that the net is not in a tight manner. In both the Large-Scale Map and Map Information Production Regulation and the 1/2500 Large Scale Map Production Regulation, which was abolished, the traverse nets created must be stretched. In the event that the net is disturbed for compulsory reasons, there is no problem in the coordinate calculation of the traverse unless a rough error is made in the size of the edge and angle. However, if a rough error is made in the angle or edge dimension on a non-taut traverse net, is it possible to determine the point where the rough faulty edge or rough faulty angle is measured with the taught rules? Whether this is possible or not was investigated in this study. In this study, theoretical information on the subject has been given and practical studies have been done. Findings and opinions obtained as a result of the study are stated.

## 1. Introduction

When a traverse net is in a taut position, the angles measured between the directions observed at the traverse points are close to 200°. If the angles measured between the directions observed at the traverse points are around 100° or 300°, this indicates that the net is not in a taut manner. A limitation has been imposed on the length of the net in order to ensure tautness in the traverse nets both in the Large-Scale Map and Map Information Production Regulation and in the abolished Large-Scale Map and Map Information Production Regulation.

For the total length of the traverse net, it must not exceed 1.5 times the length between the start and end points of the net. The formulas developed for the investigation of the coarse faulty edge and coarse faulty angle in the polygon [1-7] were developed for taut nets.

In practice, sometimes there are cases where the above requirement for taut nets cannot be fulfilled due to terrain conditions. A question may come to mind. What harm can it be to create a non-taut traverse net with a rough faulty edge or a faulty angle to the rough, in case of necessity. In such cases, if the angles and edges of the traverse are measured more carefully, there will be no abnormal situation in traverse coordinate calculations.

However, if a rough error is made in the edge size or angle measurement on a non-taut traverse net, how long are the rules for investigating the rough error in taut nets.

In a study conducted on this subject [3], information was obtained about the investigation of the rough defective edge on a non-taut traverse net, but a study on the investigation of the rough defective angle on a non-taut traverse net was not found in the literature [8-17].

This study was carried out in order to explain the situations that occurred during the investigation of a rough error in the edge size of a non-taut traverse net and to investigate the effects of a rough error in the angle size on this specified net. Theoretical information on the subject has been given and practical studies have been made, and the findings and opinions obtained as a result of the study have been stated.

## 2. The effect of a non-taut traverse net shape on the investigation of a roughly faulty edge

A coarse faulty edge on a taut traverse net may have been measured longer or shorter than its exact value. In the investigation of rough faulty edge on the traverse net; It is first investigated whether the rough faulty edge is measured longer or shorter than its exact value.

In Figure 1;

$$[\Delta Y] = \Delta Y_1 + \Delta Y_2 + \dots + \Delta Y_n \quad (1)$$

$$[\Delta X] = \Delta X_1 + \Delta X_2 + \dots + \Delta X_n \quad (2)$$

$$\overline{\Delta Y} = Y_C - Y_B \quad (3)$$

$$\overline{\Delta X} = X_C - X_B \quad (4)$$

$$\overline{BC'} = \sqrt{([\Delta Y]^2 + [\Delta X]^2)} \quad (5)$$

$$\overline{BC''} = \sqrt{([\Delta Y]^2 + [\Delta X]^2)} \quad (6)$$

$$\overline{BC} = \sqrt{(\overline{\Delta Y}^2 + \overline{\Delta X}^2)} \quad (7)$$

$$f_y = \overline{\Delta Y} - [\Delta Y] \quad (8)$$

$$f_x = \overline{\Delta X} - [\Delta X] \quad (9)$$

$\overline{BC'} > \overline{BC}$  if the coarse faulty edge is measured longer than its absolute value,  
 $\overline{BC''} < \overline{BC}$  if the rough edge is measured shorter than the absolute value.

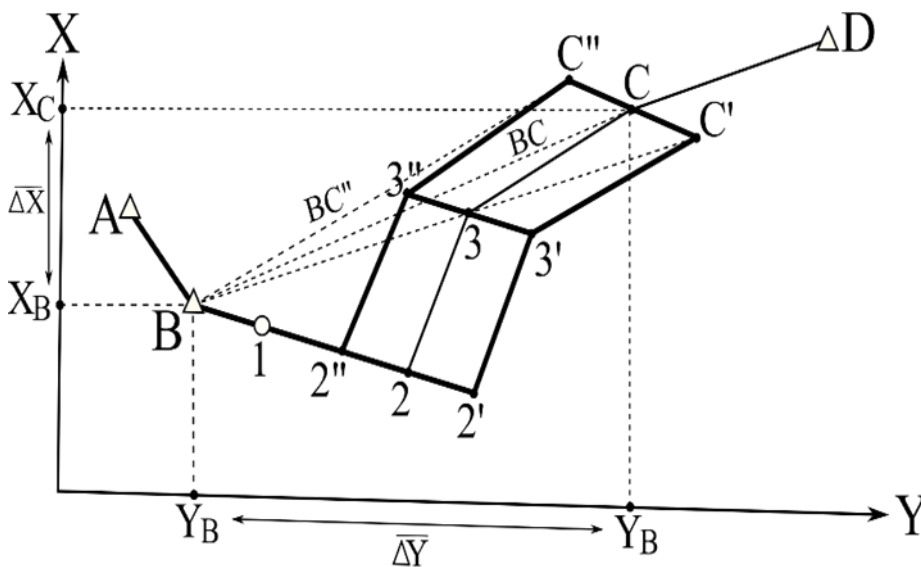


Figure 1. Schematic view of  $\overline{BC}$ ,  $\overline{BC'}$  and  $\overline{BC''}$  in the form of a taut traverse net.

After determining the condition of the rough faulty edge, to find the approximate bearing angle of the rough faulty edge:

$$(CC') = \arctan \left( \frac{-fy}{-fx} \right) \quad (10)$$

If the coarse faulty edge is measured longer than its absolute value, the following equation is applied.

$$(CC') = \arctan \left( \frac{-fy}{-fx} \right), (C''C) = \arctan \left( \frac{fy}{fx} \right) \quad (11)$$

If the coarse faulty edge is measured shorter than its exact value  $(C''C) = \arctan (fy / fx)$  (11) relation applies [3].

If the bearing angle calculated from Equation (10) or (11) is approximately equal to the bearing angle of which edge in the polygon coordinate calculation chart, that edge is the rough faulty edge. If the shape of the traverse net is not taut and the rough error is made at the edge where the net tautness is distorted the most (Figure 2), the following situations are seen in the rough error edge investigation:

- 1-When the effect of an edge measured longer than its absolute value with coarse errors, on the (C) position of the end point of the net is examined, it should be  $\overline{BC'} > \overline{BC}$ , while  $\overline{BC'} < \overline{BC}$  situation is encountered.
- 2-When the effect of an edge measured shorter than its absolute value with rough error on the position (C) of the end point of the net is examined, it should be  $\overline{BC''} < \overline{BC}$ , while  $\overline{BC''} > \overline{BC}$  situation is encountered.

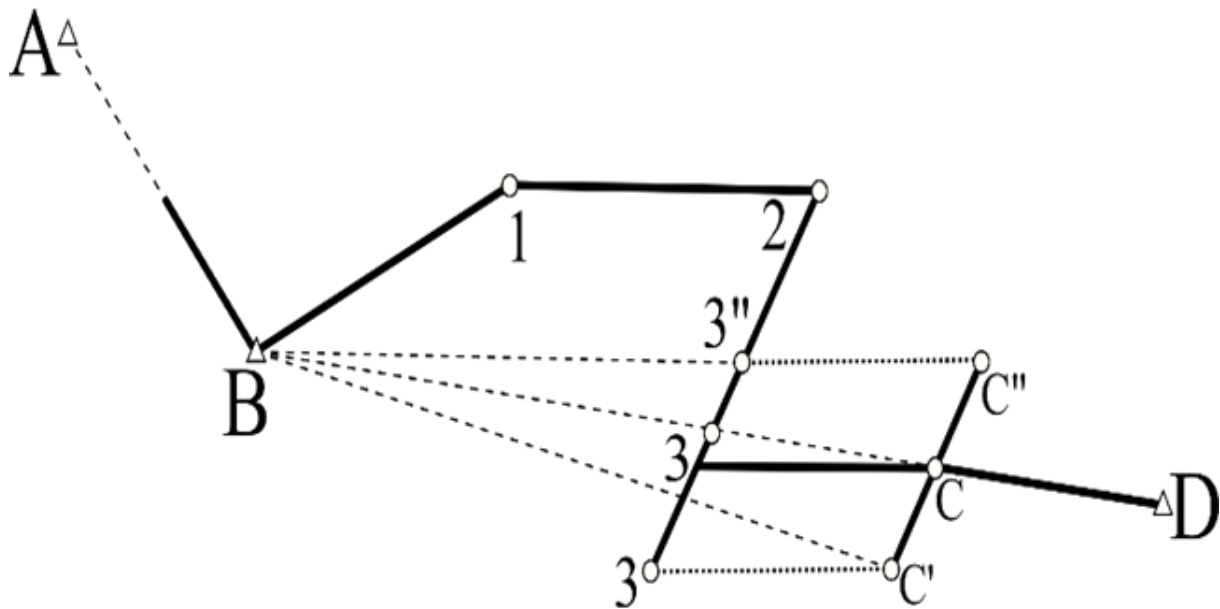


**Figure 2.** The effect of a rough error on an edge that deviates significantly according to the direction of the route on the position of the end point of the net (Schematic view of  $(\overline{BC}, \overline{BC'} \text{ and } \overline{BC''})$ )

If the shape of the traverse net is not taut and the rough error is made at an edge where the net tautness is not disturbed (Figure 3), the effect of this rough error on the position of the end point of the net is similar to that of the taut net.

In other words, if the coarse faulty edge is measured longer than its exact value,  $\overline{BC'} > \overline{BC}$  condition and if the coarse faulty edge is measured shorter than its absolute value,  $\overline{BC''} < \overline{BC}$  condition is in question.

In Figure 3; The district obtained by Equations (10) or (11) because a misleading situation is encountered as  $\overline{BC''} > \overline{BC}$  or  $\overline{BC'} > \overline{BC}$  even though the rough error edge is measured longer or shorter than the absolute value angle will not reflect the actual situation.

In other words, it will not be possible to reach a definite conclusion from the provisions stated in the rough error edge search for taut traverse nets [3]. In this case, the measure of all sides on the traverse net will be repeated.

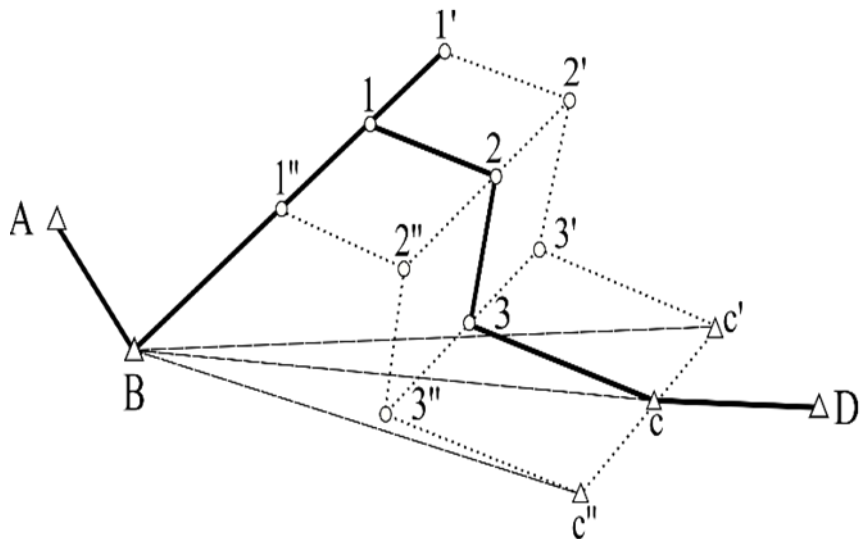


**Figure 3.** The effect of a rough error on an edge of the net that does not deviate significantly according to the direction of the net on the position of the end point of the net (Schematic view of  $\overline{BC}$ ,  $\overline{BC'}$  and  $\overline{BC''}$ )

**3. The effect of a non -taut traverse net shape on the investigation of a roughly incorrect angle**

In the graphical investigation of a rough error in angle measurement in a taut traverse net, the traverse points on the net are drawn on a plan according to their coordinates according to a determined scale. In the created plan, the middle perpendicular of the line, which combines the real position of the point where the traverse net is connected and its erroneous position, passes through the point where the wrong angle to the rough is measured [1], (Figure 4).

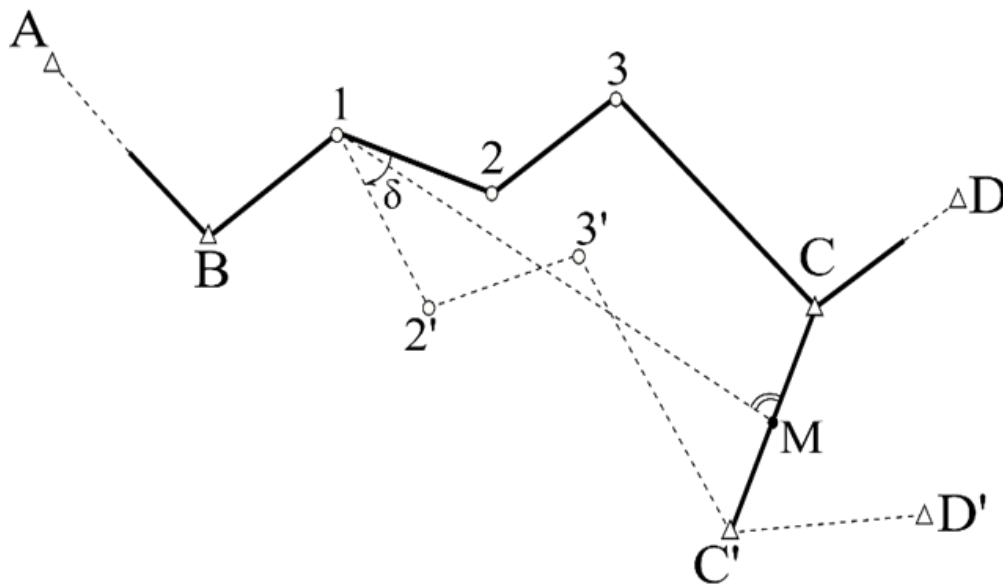


**Figure 4.** Graphically investigating the point where a rough erroneous angle is measured on the taut traverse net.

The following equations are applied in the investigation of the point where the rough angle is measured with the one-way calculation method.

$$Y_M = \frac{Y_C + Y'_C}{2}, \quad X_M = \frac{X_C + X'_C}{2} \tag{12}$$

$\delta$  = Angle-closing error exceeding the error limit to be

$$Y_P = Y_M - 0.5 * \frac{(X'_C - X_C)}{\tan(\frac{\delta}{2})} \tag{13}$$

$$X_P = X_M + 0.5 * \frac{(Y'_C - Y_C)}{\tan(\frac{\delta}{2})} \quad (14)$$

The  $Y_P$  and  $X_P$  values calculated from the Equations (13) and (14) are compared with the coordinate values calculated in the polygon coordinate spreadsheet. The coordinate of which point in the polygon spreadsheet is approximately equal to the value of  $Y_P$  and  $X_P$ , the point where the rough angle is measured is that point. In the graphical detection of the rough error made in the angle measurement in a polygon on a non-taut traverse net, the following situation occurs in the above-mentioned plan. In this case, the middle perpendicular of the line that combines the real position of the point where the net is connected and its erroneous position does not pass through the point where the rough angle is measured (Figure 5). That is, in this case, it is not certain as in the taut net, the specified middle strut passes as shifted from the rough wrong point.

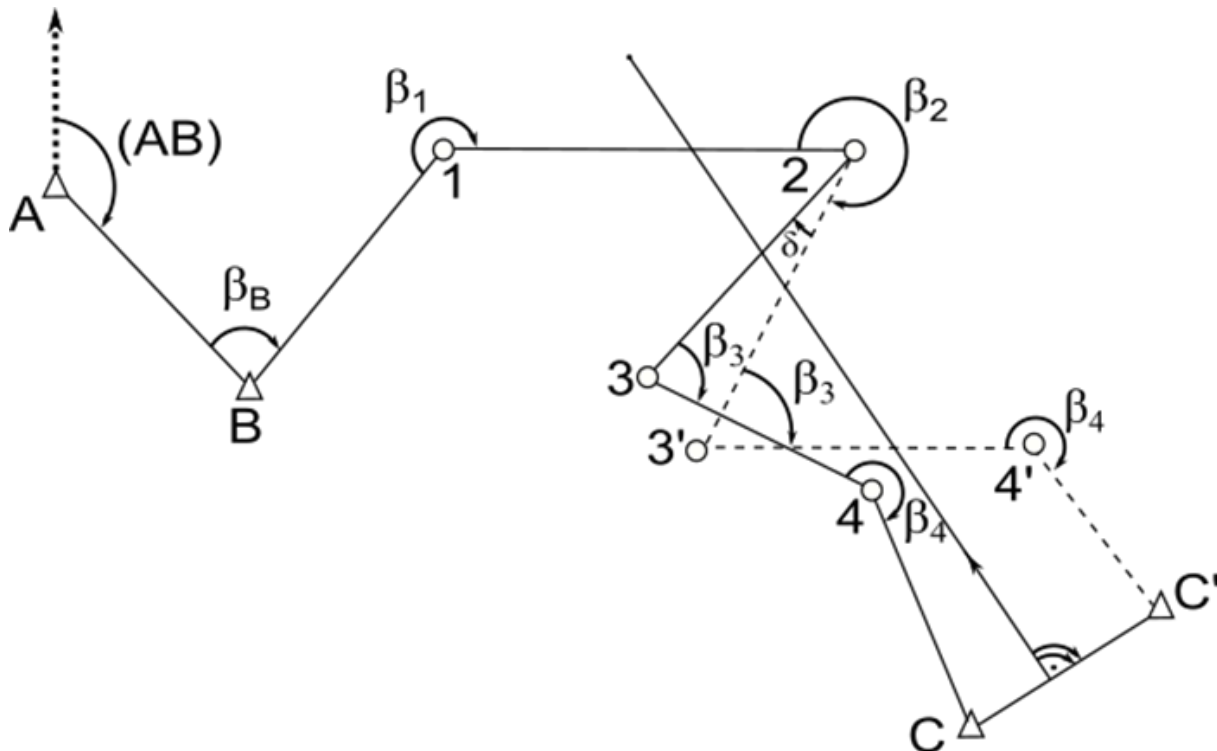


**Figure 5.** Graphically investigating the point where a rough erroneous angle is measured in the non-taut traverse net.

In this case, the  $Y_P$ ,  $X_P$  coordinates obtained by the one-way calculation method are not very close to any of the coordinates calculated in the polygon coordinate spreadsheet. In this case, it will be necessary to use the only solution, two-way calculation method in investigating the gross error.

#### 4. Numerical application

##### 4.1. Applications related to coarse faulty edge investigation

In reality, a traverse net is taken into account, with angle measurements and edge dimensions without rough error and non-taut. It has been determined according to the formulas given below that the angle closure error, transverse closing error and longitudinal closing error do not exceed their error limits. In this given net (Figure 6), it was assumed that the two edges shown as an example were measured as longer and shorter than the exact value, and a rough faulty edge investigation was made.

Traverse angles;  
 $\beta_B=152.1790$   $\beta_1=224.3075$ ,  $\beta_2=375.7624$ ,  $\beta_3=45.8265$ ,  $\beta_C=242.3288$ ,  
 Bearing angles:  
 (AB)= 125.3843 and (CD)= 165.7744  
 Traverse edges:  
 $S_1 = 320.50$  m,  $S_2=350.36$ ,  $S_3=180.65$ ,  $S_4=345.86$   
 $Y_B= 29650.52$ m,  $X_B=30584.92$ ,  $Y_C=30454.48$ ,  $X_C=30498.66$

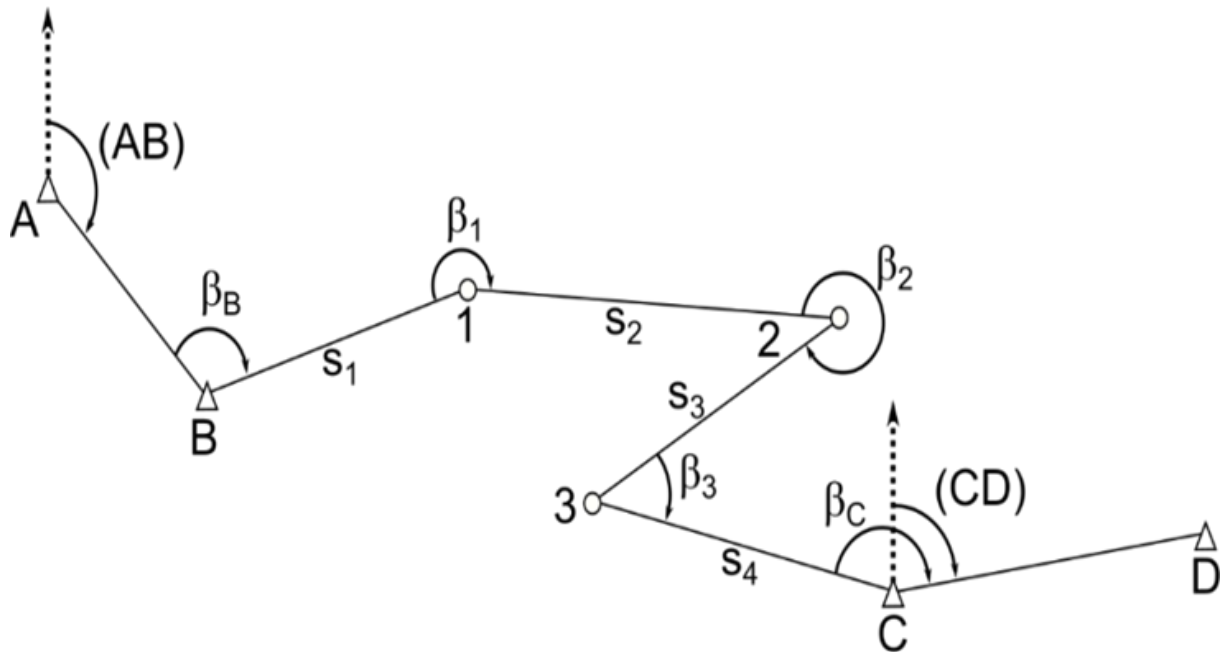


**Figure 6.** Graphically investigating the point where a rough erroneous angle is measured in the non-taut traverse net.

**Table 1.** Traverse coordinate spreadsheet with roughly accurate measurements.

Point Number	Traverse Angle ( $\beta$ )	Bearing Angle	Edge	Y $\Delta Y$	X $\Delta X$
A				29650.52	
B	-28 <sup>cc</sup> 152.1790	125.3843			30584.92
P.1	-28 <sup>cc</sup> 224.3075	77.5605	320.50	-3 300.80	-2 110.64
P.2	-28 <sup>cc</sup> 375.7624	101.8652	350.36	-3 350.21	-2 10.26
P.3	-28 <sup>cc</sup> 45.8265	277.6248	180.65	-169.61	-2 -62.19
C	-29 <sup>cc</sup> 242.3288	123.4485	345.86	-3 322.66 30454.48	-2 -124.53 4382.63 30498.66
D		165.7744 <u>-165.7885</u>	[S]=687.15	$\overline{\Delta Y} = 803.96$ [ $\Delta Y$ ]=804.06	$\overline{\Delta X} = -86.26$ [ $\Delta X$ ]=-86.34
(AB)+[ $\beta$ ]	1165.7885	$f_\beta = -0.0141$	141/5=28 +1	$f_y = -0.10$	$f_x = -0.08$
n*200=	-1000.0000				
(CD)'	165.7885				
Controls		$F_{\beta_{max}} = 1^c + \frac{150}{[S]} \cdot (n-1) \cdot \sqrt{n} = 2.12^c$		$S = \sqrt{[\Delta Y]^2 + [\Delta X]^2} = 268.32 \text{ m}$	
$f_s = \sqrt{f_y^2 + f_x^2} =$		$F_Q = 0.06 + 0.00007 \cdot S + 0.007 \cdot n \cdot \sqrt{n} = 0.17 \text{ m}$		$f_Q = \frac{1}{S} \cdot (f_y \cdot [\Delta X] - f_x \cdot [\Delta Y]) = 0.15 \text{ m}$	
$\sqrt{f_L^2 + f_Q^2} = 0.153 \text{ m}$		$F_L = 0.06 + 0.00015 \cdot S + 0.004 \cdot \sqrt{S} = 0.23 \text{ m}$		$f_L = \frac{1}{S} \cdot (f_y \cdot [\Delta Y] - f_x \cdot [\Delta X]) = 0.04$	

**Numerical Application 1:** Suppose that in Figure 6, which is actually without rough error, 300.40m is measured as shorter than the exact value of 12 edges (350.36 m).

**Solution 1:**

$$\begin{aligned} \Delta Y_1 &= 300.40 \cdot \sin 101.8652 = 300.27 \text{ m}, \\ \Delta X_1 &= 300.40 \cdot \cos 101.8652 = -8.80 \text{ m} \\ [\Delta Y] &= 300.80 + 300.27 - 169.61 + 322.66 = 754.12 \text{ m} \\ [\Delta X] &= 110.64 - 8.80 - 62.19 - 124.53 = -84.88 \text{ m} \\ f_y &= 803.96 - 754.12 = 49.84 \text{ m}, \quad f_x = -86.26 - (-84.88) = -1.38 \text{ m} \end{aligned}$$

$$BC = \sqrt{(803.96^2 + 86.26^2)} = 808.574 \text{ m}, \quad BC' = \sqrt{(754.12^2 + 84.88^2)} = 758.882 \text{ m}$$

BC' < BC condition is in question.

$$(C''C) = 200 - \arctan\left(\frac{49.84}{1.38}\right) = 101.7623, \quad C''C = \sqrt{(49.84^2 + 1.38^2)} = 49.86 \text{ m}$$

For the test, the approximate bearing angle value of the edge, which was taken deliberately short from its exact value, was obtained. In this non-taut net, the difference of  $\pm 200$ g of the calculated (C''C) bearing angle is not approximately equal to the bearing angle of the edge of the net (277g.6248 in Chart 1) that makes a significant deviation in the direction of the net. For this reason, the rough error should be investigated on the edge, which is approximately equal to the bearing angle (CC').

**Numerical Application 2:** Suppose in Figure 6, which is actually without rough error, 23 edges are measured 210.65 m longer than its exact value.

**Solution 2:**

$$\begin{aligned} \Delta Y_3 &= 210.65 \cdot \sin 277.6248 = -197.77 \text{ m}, \\ \Delta X_3 &= 210.65 \cdot \cos 277.6248 = -72.52 \text{ m} \\ [\Delta Y] &= 300.80 + 350.21 - 197.77 + 322.66 = 775.90 \text{ m} \\ [\Delta X] &= 110.64 - 10.26 - 72.52 - 124.53 = -96.67 \text{ m} \\ f_y &= 803.96 - 775.90 = 28.16 \text{ m}, \quad f_x = -86.26 - (-96.67) = 10.33 \text{ m} \end{aligned}$$

$$BC = \sqrt{(803.96^2 + 86.26^2)} = 808.574 \text{ m}, \quad BC' = \sqrt{(775.90^2 + 96.67^2)} = 781.899 \text{ m}$$

BC' < BC condition is in question.

$$(C''C) = \arctan\left(\frac{28.16}{10.33}\right) = 77.6170, \quad C''C = \sqrt{(28.16^2 + 10.33^2)} = 29.995 \text{ m}$$

Since (B1) is '(CC)', it is decided that the wrong edge is the B1 edge. However, if there was a taut net, it would have been BC' > BC and therefore (CC') = 277.6170. In this non-taut net, it is seen that the  $\pm 200$ g difference of the (CC') bearing angle is approximately equal to the bearing angle (277g.6248) of the edge of the net, which deviates significantly according to the calculation direction in the study in Chart 1. In this case, it will be necessary to repeat the measurement of edge 23 as the rough faulty edge and edge B1 for checking.

**4.2. Applications of coarse faulty angle survey**

In reality, a traverse net is taken into account, with angle measurements and edge dimensions without rough error and non-taut. It has been determined according to the formulas given below that the angle closure error, transverse closing error and longitudinal closing error do not exceed their error limits. In this given net (Figure 7), it was assumed that the angle at the one point shown as an example was measured in error to the rough, and the investigation of the rough incorrect angle was carried out using the one-way calculation method.

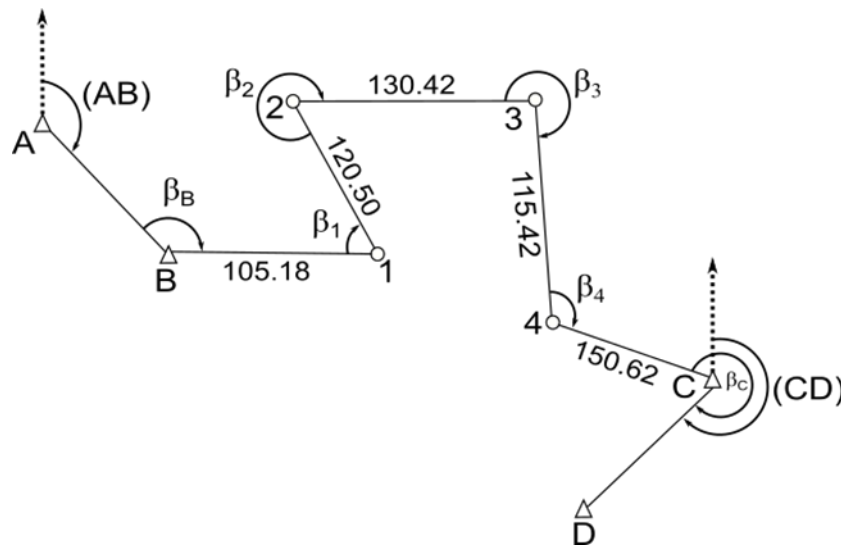


Figure 7. A non-taut traverse net

Traverse angles:  $\beta_B=165.2250$ ,  $\beta_1=65.6672$ ,  $\beta_2=353.2789$ ,  $\beta_3=286.1350$ ,  $\beta_4=165.3614$ ,  $\beta_C=301.4250$   
 Traverse edges:  $S_1=105.18$  m,  $S_2=120.50$ ,  $S_3=130.42$ ,  $S_4=115.42$ ,  $S_5=150.62$  m  
 $Y_B=2000.00$  m,  $X_B=2000.00$ ,  $Y_C=2221.60$ ,  $X_C=1809.76$  m

Table 2. Polygon coordinate calculation chart.

Point Number	( $\beta$ ) Traverse Angle	Bearing Angle	Edge	Y $\Delta Y$	X $\Delta X$
A	-32				
B	65.2250	136.3740		2000.00	2000.00
P.1	-32 5.6672	101.5958	105.18	105.15 2105.15	-1 1997.35
P.2	353.2789	367.2598	120.50	+1 -59.28 2045.88	-1 104.91 2102.25
P.3	-33 286.1350	120.5365	130.42	+1 123.69 2169.58	-1 -41.35 2060.89
P.4	-33 65.3614	206.6682	115.42	+1 -12.07 2157.52	-1 -114.79 1946.09
C	-33 301.4250	172.0263	150.62	+1 64.07 2221.60	-2 -136.31 1809.76
D	1473.4665 1200.0000	273.4470 -273.4665 $\delta=-0.0195$	[S]=687.15	$\overline{\Delta Y}=221.60$ [ $\Delta Y$ ]=221.56 fy=0.04	$\overline{\Delta X}=-190.25$ [ $\Delta X$ ]=-190.19 fx=-0.06

The net tautness condition specified in the New Large-Scale Map and Map Information Production Regulation is examined according to the following correlations.

$$BC = \sqrt{(221.60^2 + 190.25^2)} = 292.06 \text{ m}$$

$$[S] = 687.15 < 1.5 * BC = 438.10$$

Since  $[S] > 1.5 * BC$  at the end of the calculation, this traverse net is non taut since the required  $[S] < 1.5 * BC$  condition is not met.

**Numerical Application 3:** Suppose that, from the data in Figure 6, the angle at the P3 point, which is actually without rough error, is measured as 286.6350.

**Solution 3:**

**Table 3.** Coordinate Spreadsheet of a traverse net that is not in a tight shape

Point Number	(β) Traverse Angle	Bearing Angle	Edge	Y ΔY	X ΔX
A					
B	165.2250	136.3740		2000.00	2000.00
P.1	65.6672	101.5990	105.18	105.15	-2.64
P.2	353.2789	367.2662	120.50	-59.26	104.92
P.3	287.6350	120.5451	130.42	123.69	-41.36
P.4	165.3614	208.1801	115.42	-14.79	-114.47
C	301.4250	173.5415	150.62	60.81	-137.80
D	1473.4665 1200.0000	273.4470 <u>-273.9665</u>	[S]=687.15	2221.60 2215.60	1809.76 1808.65
				$Y_M=(2221.60+2211.98)/2=2218.60$	
				$X_M=(1809.76+1807.35)/2=1809.205$	
				$Y_P=Y_M-0.5*(X_C-X_C)/\tan(\delta/2)=2172.10\text{ m}$	
				$X_P=X_M+0.5*(Y_C-Y_C)/\tan(\delta/2)=2060.57\text{ m}$	
				$\delta=-0.5195$	

The closest value to the calculated  $Y_P$  value is 2167.94 m in the traverse coordinate spreadsheet and the closest value to the  $X_P$  value is 2059.97 m. In this case, the point where the rough angle is measured is the P.3 point. Although there is little between the X value and the  $X_P$  values of the coarse error point P.3, the difference between the Y value and the  $Y_P$  values is 2.52 m.

**Numerical Application 4:** Suppose that, from the data in Figure 6, the angle at the P3 point, which is actually without rough error, is measured as 287.1350.

**Solution 4:** The coordinates obtained as a result of the calculation are shown in Table 4.

**Table 4.** Coordinate Spreadsheet of a non-taut traverse net

Point Number	(β) Traverse Angle	Bearing Angle	Edge	Y ΔY	X ΔX
A					
B	165.2250	136.3740		2000.00	2000.00
P.1	65.6672	101.5990	105.18	105.15	-2.64
P.2	353.2789	367.2662	120.50	-59.26	104.92
P.3	286.0350	120.5451	130.42	123.69	-41.36
P.4	165.3614	206.5801	115.42	-11.91	-114.80
C	301.4250	171.9415	150.62	64.26	-136.23
D	1473.4665 1200.0000	273.4470 <u>-273.3665</u>	[S]=687.15	2221.60 2221.93	1809.76 1809.89
				$Y_M=(2221.60+2211.98)/2=2221.765$	
				$X_M=(1809.76+1807.35)/2=1809.825$	
				$Y_P=Y_M-0.5*(X_C-X_C)/\tan(\delta/2)=2214.11\text{ m}$	
				$X_P=X_M+0.5*(Y_C-Y_C)/\tan(\delta/2)=1829.27\text{ m}$	
				$\delta=1.0805$	

The closest value to the calculated Y<sub>P</sub> value is 2167.94 m in the polygon coordinate spreadsheet and the closest value to the X<sub>P</sub> value is 2059.97 m. In this case, the point where the rough angle is measured is the P.3 point. The difference between the X value and the X<sub>P</sub> values of the coarse faulty point P.3 is very large (231.65) and the difference between the Y value and the Y<sub>P</sub> values is 44.53 m.

## 5. Discussion

For the research, the correct coordinates of a point, whose polygon angle was deliberately taken to the grid, and the coordinates obtained from the Equations (13) and (14) were examined. In the examination, a variation curve shown in Figure 7 for dy values according to  $\delta$  rough error angle value and a change curve seen in Figure 8 for dx values were obtained. When the figures were examined carefully, it was seen that dy and dx errors occurring at small values of  $\delta$  were at the maximum value.

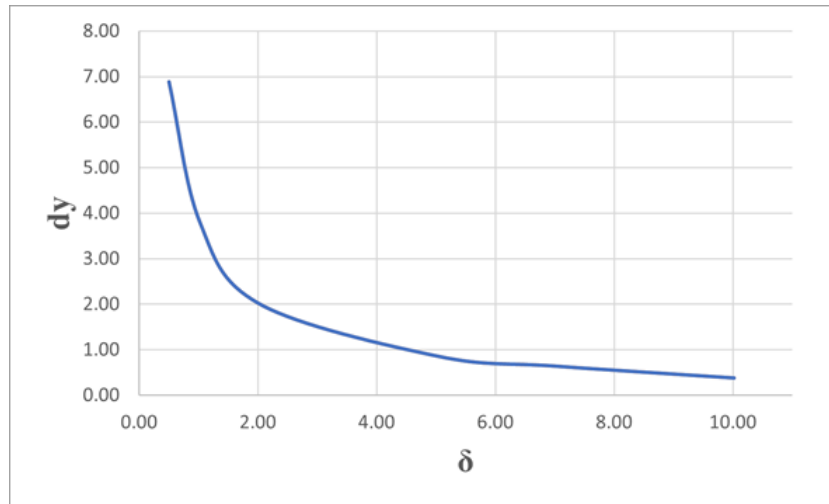


Figure 7. dy values according to  $\delta$  rough error angle value

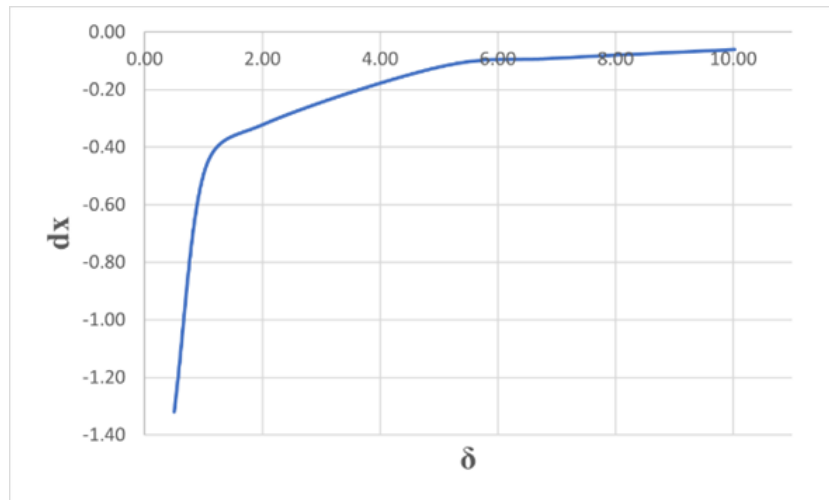


Figure 8. dx values according to  $\delta$  rough error angle value

## 6. Results

- If a rough error is made on an edge that does not deviate significantly from the direction of the net on a non-taut traverse net, it is possible to detect the rough error by applying the rules specified in the investigation of the rough faulty edge in taut net.
- In a non-taut traverse net, if a rough error is made on an edge that deviates significantly from the direction of the net, it is not possible to detect the rough error by applying the rules specified in the investigation of the rough faulty edge in taut nets.
- This situation can be explained better by the following equations. On a net from B to C,
- $BC = \sqrt{(\Delta Y_{BC}^2 + \Delta X_{BC}^2)}$ ,  $BC' = \sqrt{([\Delta Y]^2 + [\Delta X]^2)}$  If the coarse is measured longer than the edge absolute value,  $BC' > BC$  should be the misleading  $BC' < BC$  condition.

- Similarly, if the coarse faulty edge is measured shorter than its precise value,  $BC'' < BC$  should be  $BC'' > BC$  misleading situation is encountered.
- In this case, since it is not known on which edge the coarse faulty edge was measured, it will be necessary to investigate the faulty edge on many sides of the net.
- In a non-taut traverse net, if there is a rough error in the angle of an angle at a point that deviates or does not significantly deviate from the direction of the net, it is difficult to determine the rough defective point by applying the rules specified in the investigation of the rough defective angle on the taut nets.
- In the research, differences of up to  $\pm 200$  m were observed between the exact coordinates of the coarse error point and the coordinate values calculated by Equations (13) and (14). In this case, the bidirectional traverse coordinate calculation method should be applied to reveal the rough error point.
- If it is necessary to create a non-taut traverse net, great care should be taken when measuring the traverse angles and edges in order to avoid the above-mentioned situations.

## Funding

This research received no external funding.

## Author contributions

**Yener Türen:** Conceptualization, Methodology, Software **Hüseyin İnce:** Data curation, Writing-Original draft preparation, Software, Validation. **Nuri Erdem and Tuna Erol:** Visualization, Investigation, Writing-Reviewing and Editing.

## Conflicts of interest

The authors declare no conflicts of interest.

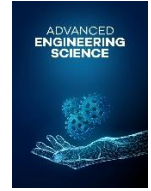
## References

1. Brönnimann, (1888). Study on The Gross Error Angles of Traverse Calculations (in German: Auffindung eines groben Winkelfehlers in einem Polygonzug) Zfv. p.524
2. Hamacher, W. (1963). Study on The Error Point of The Gross Error Angels of The Traverse Calculation (in German: Das Auffinden des Fehlerpunktes bei einem groben Winkelfehler im Polygonzug), Zfv, Nr, 3/1963, p.130-132
3. İnce, H. (1999). The Proposals in The Researching by Calculation Method of The Length Which Has Gross Error on The Dependent Traverse and Series Triangulation (in Turkish: Bağlı Poligon Ve Dizi Nirengide Kaba Hatalı Kenarın Hesap Metoduyla Araştırılmasında Öneriler), K.T.Ü. Faculty of Engineering & Architecture, Faculty Press No: 24, Trabzon, Turkey
4. Koç, İ. (1986). The Determination of Gross Error Angles by Single Calculation Method on The Traverse (in Turkish: Poligon Geçkilerinde Kaba Aç Hatasının Tek Yönlü Hesapla Bulunması), Bulletin of Chamber of Surveying Engineers, No:56-57, Ankara, Turkey
5. Pektekin, A. (1978). Calculating the Coordinates of a Traverse by Computers and Searching of Gross Error Angle and Length (in Turkish: Poligon Hesaplarının Bilgisayarlar İle Yapılması Kaba Kenar Ve Aç Hatalarının Araştırılması), Y.T.Ü. Text Nots / Monografiler, İstanbul, Turkey
6. Pinkwart, (1941). Study on The Gross Error Angles of The Conecting Traverse Calculations (in German: Die Auffindung eines groben Winkelfehlers im Polygon- zug ohne Abschlusrichtung.) Zfv. p. 227
7. Rennebach, (1941). The Determination of Gross Error Angles and Error Points in The Traverse Calculation (in German: Ermittlung eines groben Winkelfehlers und des Fehlerpunktes im Streckenzuge (Polygonzuge) ohne Abschlusrichtung). Zfv, p.81
8. Kissam, P. (1966). Surveying Practice the Fundamentals Of Surveying, McGraw- Hill, New York
9. Allan, A. L., Hollwey, J. R., Maynes, J. H. B. (1968). Pratical Field Surveying and Computations, Heinemann, London
10. Uren, J., Price, W.F. (1986). Surveying for Engineers, Second Edition, ELBS Macmillan, London
11. Kahmen, H., Faig W. (1988). Surveying, de Grayter Berlin-Newyork, ISBN 3-11-008303-5, p.259-271
12. Bannister, A., Raymond, S., Backer, R. (1992). Surveying, John Willey & Sons. Inc. 605 third Avenue, New York, p.201-206

13. Muskett, J. (1995). Site Surveying, Second Edition, Blackwell Science Ltd. Oxford ISBN 0-632-3848-9, p.100-113
14. Kavanagh, B. F. (1997). Surveying with Construction Application, 3rd Edition, Prentice Hall, USA, New Jersey, ISBN 0-13- 449679-5, p. 165-169
15. Kavanagh, B. F., Bird, S. J. G. (2000). Surveying Principles and Applications, Upper Saddle River, New Jersey 07458
16. Kavanagh, B. F. (2003). Geomatics, Pearson Education Inc. New Jersey 2003, p.156-160
17. Wolf, P. R., and Ghilani, C. D. (2008). Elementary Surveying an Introduction to Geomatics. 12th Edition, Upper Saddle River, New Jersey: Pearson Prentice-Hall. pp. 233-269



© Author(s) 2021. This work is distributed under <https://creativecommons.org/licenses/by-sa/4.0/>



## Kinetic and structural study on CuAlMnNi shape memory alloy with a novel composition

Oktaý Karaduman\*<sup>1</sup>, İskender Özkul<sup>2</sup>, Canan Aksu Canbay<sup>1</sup>

<sup>1</sup>Firat University, Faculty of Science, Department of Physics, Elazığ, Türkiye, [okinist@hotmail.com](mailto:okinist@hotmail.com); [caksu@firat.edu.tr](mailto:caksu@firat.edu.tr)

<sup>2</sup>Mersin University, Engineering Faculty, Mechanical Engineering Department, Mersin, Türkiye, [iskender@mersin.edu.tr](mailto:iskender@mersin.edu.tr)

Cite this study: Karaduman, O., Özkul, İ., & Canbay, C. A. (2021). Kinetic and structural study on CuAlMnNi shape memory alloy with a novel composition. *Advanced Engineering Science*, 1,13-19.

### Keywords

CuAlMnNi  
Shape memory alloy  
Martensite  
DSC  
DTA  
Temperature lag

### Research Article

Received: 02.05.2021

Revised: 28.06.2021

Accepted: 05.07.2021

Published: 15.08.2021



### Abstract

In this work, a CuAlMnNi shape memory alloy with a novel composition was fabricated as cast ingot by arc melting process under vacuum. The specimens of the alloy were prepared by cutting the casted ingot alloy into small pieces. After then, all of the alloy samples were homogenized in high temperature  $\beta$ -phase region and then rapidly cooled by quenching them in iced-brine water in order to form martensite structure i.e., to bring shape memory property to the alloy. Then a batch of thermal and structural tests was carried out in order to probe shape memory effect characteristics of the CuAlMnNi alloy. By the differential scanning calorimetry (DSC) tests which were taken back-to-back at varied heating/cooling rates, the solid-solid martensitic phase transformation peaks that appeared on the DSC thermograms of the alloy during cyclic heating and cooling processes of the alloy were observed as an evidence for the entity of the shape memory effect property that exists in the alloy. The transformation temperatures of the alloy were slightly changed with the heating/cooling rate changed. By making DSC peak analyses, it is determined that the martensite and austenite phases averagely start to form at  $\sim 36$  °C and  $\sim 64$  °C, respectively. Some other transformational kinetic parameters of the alloy were also calculated. Moreover, an Af temperature lag occurred at the high heating/cooling rate of 35 °C/min, which happened mainly because of that rapid heating rate that causes the temperature signal of the DSC pan hits to the DSC detector before the signal of the alloy sample in the pan does. The differential thermal analysis (DTA) test that was run at a single heating rate demonstrated that the thermal responsive behavior of the alloy in the high temperature  $\beta$ -phase region matched the common behavior of Cu-Al based memory alloys. By performing room temperature EDS analysis, the composition of the alloy was determined. The X-ray diffraction (XRD) test performed at room temperature showed the  $\beta 1'$  and dominant  $\gamma 1'$  martensite forms that formed in the alloy and this formation was theoretically also supported by calculating the average valence electron concentration per atom (e/a) value of the alloy.

## 1. Introduction

In the research area of shape memory alloys (SMAs), a class of smart materials family, the cost-effective Cu-based shape memory alloys (e.g., CuAlMn, CuAlNi, CuZnAl SMAs) are regarded as the second-best SMAs after the most commercial and superior but far more expensive NiTi SMAs [1-3]. Therefore, the research done to study, change or improve the SMA properties of the Cu-based SMAs is one of the crowd-pulling research subjects in the research area of SMAs.

Although Cu-based SMAs have better thermal and electrical conductivity characteristics than those NiTi ones [3, 4], they have weaker shape memory effect (SME) properties and poor thermal stability and they also suffer from their brittleness that causes problems in their cold-working processes [4-7]. There are some ways researchers use to decrease brittleness and improve ductility and shape memory properties of the binary Cu-based

alloys (especially Cu-Al). One of them is to add extra one or more alloying elements (also called as grain refining elements) such as Mn, Fe, Cr, Co, Ti, Ni, Cr, B, Mg, Ce, Be etc. [1, 2, 5, 7-9].

The chemical composition and adding elements have also strong effects on the transformation temperatures of SMAs. The transformation temperatures and transformational kinetic parameters of a SMA are exceedingly dependent on its alloying composition. Even minor changes in composition lead to large variations of transformation temperatures. The demanded transformation temperatures for different specific applications of SMAs therefore can be met by SMAs with different compositions [9].

In this work, an experimental research study on an arc melted quaternary CuAlMnNi shape memory alloy with a novel composition and transformation temperatures are presented. The shape memory properties of the produced alloy were demonstrated by performing some thermal and microstructural measurements including DSC, DTA, and XRD.

## 2. Method

The CuAlMnNi SMA with a novel composition of 82Cu-12.5Al-4.5Mn-1Ni wt% (or 69.65Cu-25.01Al-4.42Mn-0.92Ni at%) was fabricated by arc melting method under argon plasma. At the beginning of the fabrication process, at first, the high purity (%99.99) metal elements of Cu, Al, Mn, and Ni powders were mixed, and then the powder mixture was pelletized under pressure. The obtained small pellets were together melted in arc melter and the as cast ingot alloy was obtained. Then small alloy samples proper for the measurements were prepared by cutting this ingot alloy. To install shape memory effect property into the alloy samples, all of them were together heat-treated in a furnace at 900 °C for 1 h for crystallographic homogenization, and at the end of this homogenization, they were immediately quenched in iced-brine water which is used as a frequent quenching method. By doing this rapid cooling from a high  $\beta$ -phase temperature region, the hypoeutectoid precipitations that would normally form by slow coolings are surpassed and therefore the martensite phase is forced to form in the alloy samples which is the base of shape memory properties. By using a Shimadzu 60A label DSC equipment, the DSC tests were taken under 10, 15, 20, 25 and 30 °C/min of heating/cooling rates between room temperature and 150 °C under a constant argon gas flow of 100 ml/min. The DTA test was performed under the same gas flow at a single 25 °C/min of heating rate from room temperature to 900 °C by using a Shimadzu DTG-60AH instrument. A Zeiss Evo MA10 model EDX instrument was used to determine the alloy composition under room conditions. The X-ray diffraction (XRD) test by using CuK $\alpha$  radiation was taken also at room temperature via using a Rigaku RadB-DMAX II diffractometer to reveal the diffraction planes of the martensite phases at room temperature.

## 3. Results

For all of the DSC heating/cooling rates, the multiple DSC heating/cooling running cycles of the produced CuAlMnNi SMA which were originally obtained from DSC software analysis program are presented in Figure 1. According to these DSC curves taken at different heating/cooling rates, the downward endothermic peaks seen on all heating fragments of these DSC cycles indicate the forward martensite to austenite (M→A) phase transitions, in other words, the  $\beta 1'$  (and  $\gamma 1'$ ) martensite transform into  $\beta 1(L2_1)$  austenite phase by the coercion of lattice internal stresses generated by heat intake (phonons) [3, 5, 10-12]. On the contrary, when looking at the exothermic peaks on the upward cooling fragments of the DSC curves, at this time the correspondent backward A→M transitions seem to have occurred. Meanwhile, on the DSC curve run at the high heating/cooling rate of 35 °C/min, an  $A_f$  temperature lag (thermal lag) [4] can be seen to have occurred in the M→A peak that appeared as a flattening in the bottom of that M→A peak. This happened mostly due to the high heating rate that leads to a delay in detection of the temperature signal comes from the alloy sample as compared to the signal comes from the DSC sample pan, the detailed reasons for this lagging temperature phenomenon is well explained in a recent work [4].

The characteristic parameters of martensitic transformation temperatures ( $A_s$ ,  $A_f$ ,  $M_s$ , and  $M_f$ ) and enthalpy change amounts ( $\Delta H_{M\rightarrow A}$ ) spent during M→A transformations for each heating/cooling rate were directly obtained as data sets by doing the DSC peak analyses on the DSC analyzer program which automatically uses the tangent differentiation method. Then, the values of the hysteresis gap ( $A_s-M_f$ ), and the values of the other related important kinetic parameters; the equilibrium temperature ( $T_0$ ), and the entropy change amounts ( $\Delta S_{M\rightarrow A}$ ) of the CuAlMnNi SMA were calculated. All of these characteristic thermodynamical parameters with their calculated average values were listed in Table 1. Plus, the changes in the parameters of transformation temperatures, hysteresis gap, and equilibrium temperature by heating/cooling rate were drawn as line graphics and presented in Figure 2.

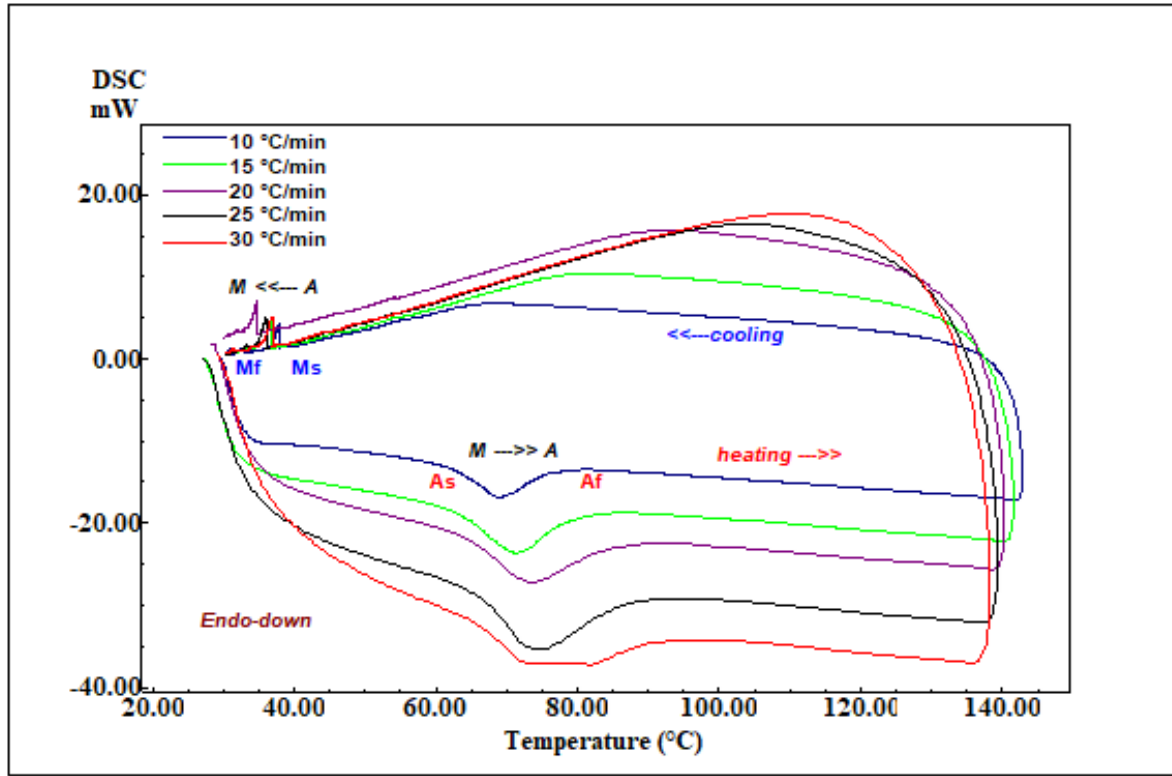


Figure 1. The multiple cyclic DSC heating/cooling curves of the produced CuAlMnNi SMA.

Table 1. The martensitic transformation temperatures and kinetic parameters of the CuAlMnNi SMA.

Heating/cooling rate (°C/min)	As (°C)	Ar (°C)	A <sub>max</sub> (°C)	Ms (°C)	Mr (°C)	As-Mr (°C)	T <sub>0</sub> (°C)	ΔH <sub>M→A</sub> (J/g)	ΔS <sub>M→A</sub> (J/g°C)
10	62.51	76.13	69.07	37.98	36.89	25.62	57.055	6.48	0.1136
15	62.43	79.47	71.30	36.74	35.73	26.70	58.105	8.06	0.1387
20	65.48	85.52	73.58	34.75	33.93	31.55	60.135	8.68	0.1443
25	66.38	87.31	74.67	36.02	34.97	31.41	61.665	8.64	0.1401
30	66.61	93.90	81.93	36.94	35.76	30.85	65.42	7.27	0.1111
Avg.	64.20	82.11	72.16	36.37	35.38	28.82	59.24	7.965	0.1342

Among the calculated kinetic parameters, the values of equilibrium temperature ( $T_0$ ) were calculated by using  $T_0=(A_r+M_s)/2$  formula [13]. The equilibrium temperature is the temperature at where the chemical free energy or the Gibbs free energy ( $G$ ) amounts of both austenite and martensite phases are equalized, which means that at this point there is no driving force affecting the alloy to any transformation direction [10]. Also, the average lattice entropy change values ( $\Delta S_{M \rightarrow A}$ ) for each endothermic  $M \rightarrow A$  transformation were found by using  $\Delta S_{A \leftrightarrow M} = \Delta H_{A \leftrightarrow M} / T_0$  relation [10]. These high enthalpies and calculated entropy values mean that the CuAlMnNi alloy has a good shape memory effect.

The activation energy ( $E_a$ ) parameter is also another important kinetic parameter for SMAs which is the required energy for both forward and backward martensitic transformations to occur. This energy determines the nature of the crystallization behavior of the SMAs. The values activation energy ( $E_a$ ) of the CuAlMnNi alloy were computed by using the Kissinger formula [10, 14] given in Equation 1;

$$\frac{d [\ln(\Phi/T_m^2)]}{d(1/T_m)} = - E_a/R \quad (1)$$

where;  $\Phi$  refers to heating/cooling rate,  $T_m$  is maximum austenite peak temperature ( $A_{max}$ ),  $R$  is the universal gas constant ( $R= 8.314 \text{ J/mol.K}$ ). The term on the left side of this equation was drawn as a plot of  $\ln(\Phi/T_m^2)$  versus  $1000/T_m$  shown in Figure 3. This plot shows how the activation energy ( $E_a$ ) changes by heating rate. By finding the slope value from applying the linear fit of this plot, and then substituting this slope value as the left term in the Equation 1, the activation energy of the alloy was calculated as 166.40 kJ/mol.

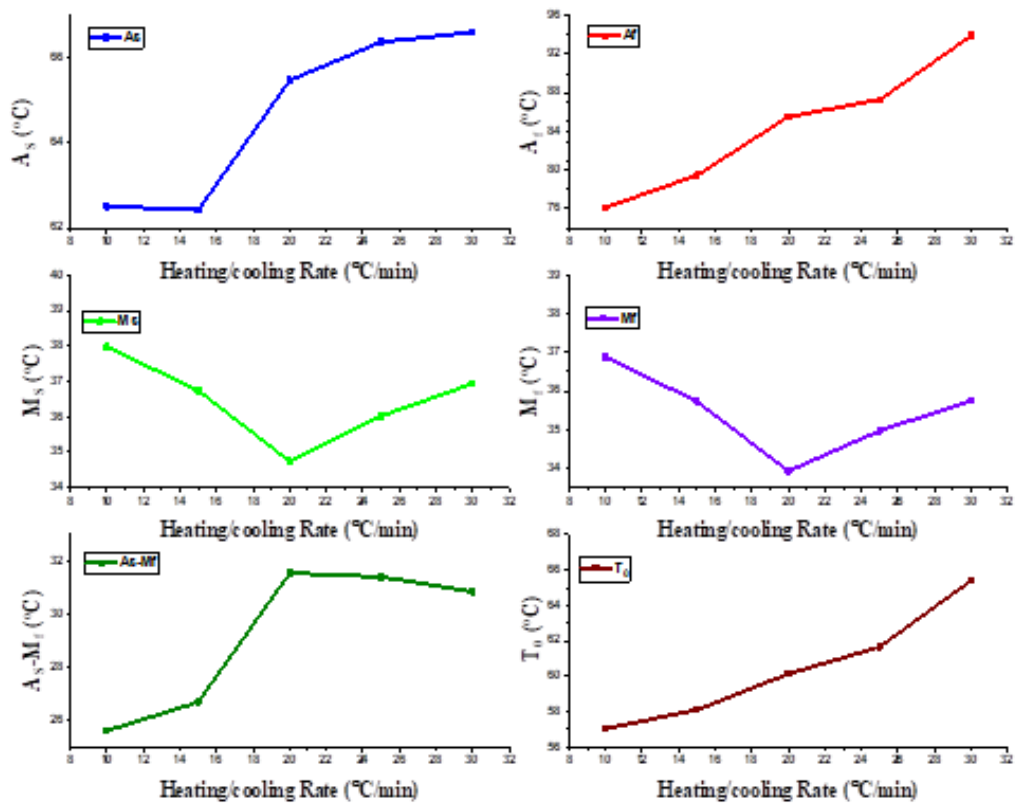


**Figure 2.** The graphics of characteristic martensitic transformation temperatures ( $A_s$ ,  $A_f$ ,  $M_s$ , and  $M_f$ ), hysteresis gap ( $A_s-M_f$ ), and equilibrium temperature versus heating/cooling rate.

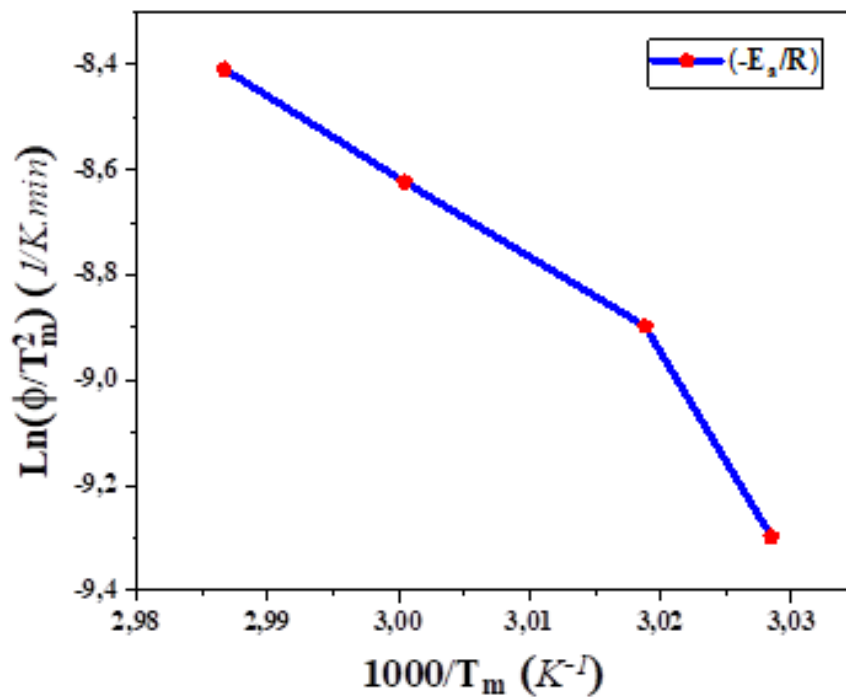


**Figure 3.** The graphic of the change in the activation energy  $E_a$ .

The DTA heating curve of the CuAlMnNi alloy obtained at the single heating rate of 25 °C/min is given in Figure 4. According to the appeared peaks observed on this DTA heating curve, the CuAlMnNi alloy exhibited multiple stages of phase transitions of  $\beta_1'(+\gamma_1') \rightarrow \beta_1(\text{DO}_3; \text{L}2_1) \rightarrow \beta_2(\text{B}_2, \text{metastable}) \rightarrow \text{hypoeutectoid } \alpha+\gamma_2 \text{ precipitations (decomposition)} \rightarrow \text{eutectoid recomposition} \rightarrow \beta_2(\text{B}_2, \text{ordered}) \rightarrow \beta(\text{A}_2, \text{disordered})$  and this common DTA pattern of Cu-based SMAs was found constant with the previous works [10, 14, 15].

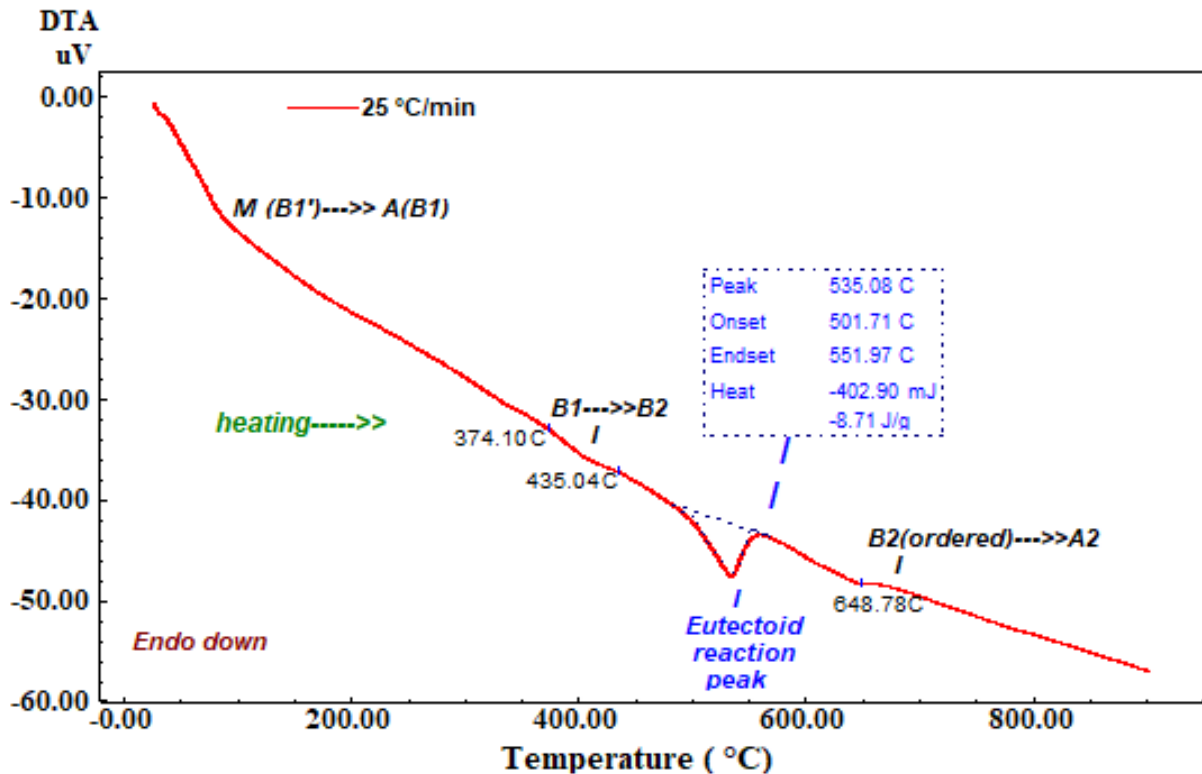


**Figure 4.** The DTA heating curve of the CuAlMnNi SMA, showing the sequential multiple stages of phase transitions behaviour of this alloy while it was heated through the high temperature  $\beta$ -phase region.

The average valence electron concentration per atom ( $e/a$ ) parameter is a key parameter for Cu-based SMAs concerning having a SME property [1, 3]. The estimation on the types and volumetric dominance of the formed martensite phases in the alloy executed through this  $e/a$  parameter can give us a theoretical prediction or a prior knowledge about the martensitic nature of the alloy texture because the vibrational entropy change ( $\Delta S$ ) of average periodic lattice formation is a function that is highly depended on the  $e/a$  parameter [1, 3, 15]. It is expressed that the Cu-based SMAs generally must have  $e/a$  concentrations between 1.45 and 1.49 (or 1.51) to have a SME property [1, 3, 10, 15]. This  $e/a$  number value range is also a determining condition for the volumetric dominance of the monoclinic  $\beta_1'$ (M18R) and the hexagonal  $\gamma_1'$ (2H) types of martensite forms so that if the  $e/a$  value of a Cu-based SMA is going below this range the  $\beta_1'$  gains dominancy over  $\gamma_1'$ , inversely as it becomes larger than this range then  $\gamma_1'$  is the dominant martensite phase, and if the  $e/a$  value is in the mid of that range then both two types of martensite forms with nearly equal volumes take place in the alloy texture interwoven [3, 10, 15, 16]. By using the atomic fractions ( $f_i$ ) of each alloying element according to the alloy composition of 69.65Cu-25.01Al-4.42Mn-0.92Ni at% and their corresponding valence electron numbers ( $v_i$ ) in the  $e/a = \sum f_i v_i$  formula [10, 11] the  $e/a$  value of the produced CuAlMnNi alloy was found as 1.55, and this value indicates that the  $\gamma_1'$ (2H) types of martensite phase must have formed in the alloy as the dominant martensite phase. This theoretical assessment or prediction on the martensitic structure of the alloy is to be verified by the structural XRD test result given below.

The XRD result showing the peaks on the diffraction pattern of the CuAlMnNi alloy labeled with the corresponding planes of both types of martensite phases can be seen in Figure 5. On this XRD pattern, it is seen that the highest diffraction peak the plane of the  $\gamma_1'$ (211) type martensite is the main diffraction peak, so this martensite is the dominant martensite (confirming the prediction made on the  $e/a$  value of the alloy), and the other observed martensite peaks are  $\gamma_1'$ (111),  $\gamma_1'$ (020),  $\gamma_1'$ (202),  $\beta_1'$ (020),  $\beta_1'$ (0022),  $\beta_1'$ (12-8),  $\beta_1'$ (2012),  $\beta_1'$ (1210),  $\beta_1'$ (208),  $\beta_1'$ (331), and  $\beta_1'$ (042) [3, 5, 10, 17-23]. Moreover, the precipitation peaks of a Cu- $\alpha$ (200) and a  $\text{Cu}_9\text{Al}_4\text{-}\gamma_1$ (444), and the austenitic  $\text{L}2_1$  phase peaks of  $\beta_1$ (200) and  $\beta_1$ (331) were observed on the XRD pattern, too [19-23]. All of the XRD diffraction peaks on the pattern seem to be broadened and which implies that the structure of the produced CuAlMnNi alloy has a highly nano-polycrystalline nature. The observed peaks are not very high and sharp, and they broadened as some conglomerations of the smaller adjacent peaks of different planes.

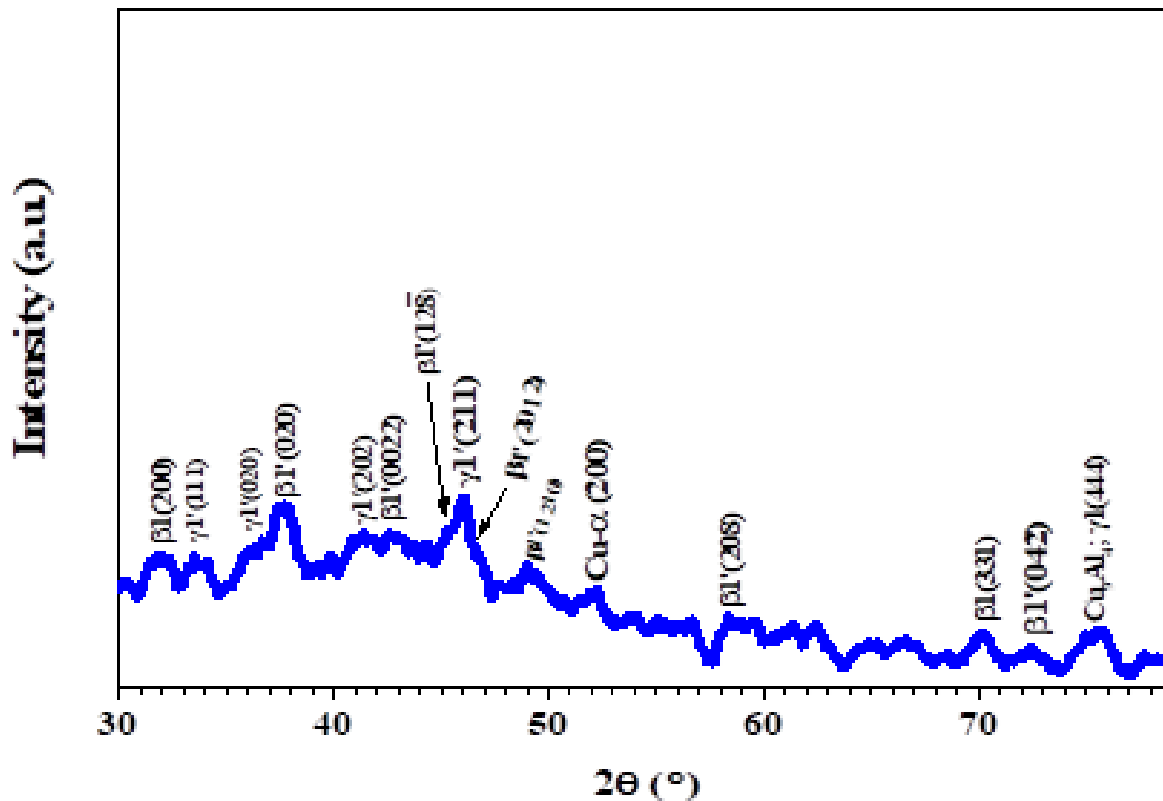


**Figure 5.** The XRD test result of the produced CuAlMnNi alloy. The peaks belong to the atomic planes of both types of interwoven martensite forms can be seen on this X-ray diffraction pattern.

#### 4. Conclusion

In this work, the CuAlMnNi shape memory alloy with a new composition was successfully fabricated by the arc melting method. The alloy was characterized by thermal and structural tests that revealed the shape memory effect property of the alloy. By DSC tests the martensitic transformation temperatures and other kinetic parameters were determined. Although the transformation temperatures slightly changed at different DSC heating/cooling rates, the alloy has average  $M_s$  and  $A_s$  temperatures of  $\sim 36$  °C and  $\sim 64$  °C, respectively. An  $A_f$  temperature lag was observed on the DSC curve at the highest heating/cooling rate, which happened due to this high rate. The high enthalpy and calculated entropy values indicated that the produced CuAlMnNi alloy has a good or powerful shape memory effect. The  $e/a$  valence electron concentration parameter of the alloy was determined as 1.55, which gave a pre-knowledge about the martensitic structure of the alloy predicting that there is a dominancy of martensite form over  $\beta_1'$  martensite form at room temperature. This prediction was affirmed by the XRD pattern of the alloy showing the highest  $\gamma_1'$  martensite peak and the other  $\gamma_1'$  and  $\beta_1'$  peaks. Some precipitations and austenite peaks were observed on the XRD pattern, too. The broadened and non-sharp XRD peaks indicated the highly polycrystalline texture of the produced alloy. In conclusion, this alloy with this new composition and transformation temperatures can be useful in many SMA and related applications.

#### Acknowledgement

This research work is a part of Ph.D. thesis works of Oktay Karaduman supervised by Assoc. Prof. Dr. Canan Aksu Canbay at Firat University, Faculty of Science, Department of Physics.

#### Funding

This research received no external funding.

#### Author contributions

**Oktay Karaduman:** Conceptualization, Methodology, Software **İskender Özkul:** Data curation, Writing-Original draft preparation, Software, Validation. **Canan Aksu Canbay:** Visualization, Investigation, Writing-Reviewing and Editing.

## Conflicts of interest

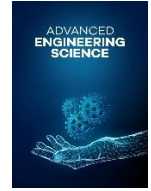
The authors declare no conflicts of interest.

## References

1. Otsuka, K., & Wayman, C. (1998). Shape Memory Materials Cambridge Univ. Press, New York..
2. Jani, J. M., Leary, M., Subic, A., & Gibson, M. A. (2014). A review of shape memory alloy research, applications and opportunities. *Materials & Design (1980-2015)*, 56, 1078-1113.
3. Canbay, C. A., & Karaduman, O. (2021). The photo response properties of shape memory alloy thin film based photodiode. *Journal of Molecular Structure*, 1235, 130263.
4. Canbay, C. A., Karaduman, O., & Özkul, İ. (2020). Lagging temperature problem in DTA/DSC measurement on investigation of NiTi SMA. *Journal of Materials Science: Materials in Electronics*, 31(16), 13284-13291.
5. Canbay, C. A., & Sampath, V. (2017). Microstructural and Thermal Investigations of Cu-Al-Mn-Ni Shape Memory Alloys. *Materials Today: Proceedings*, 4(10), 10682-10689.
6. Ahlers, M., & Pelegrina, J. (2003). Ageing of martensite: stabilisation and ferroelasticity in Cu-based shape memory alloys. *Materials Science and Engineering: A*, 356(1-2), 298-315.
7. Yang, S., Omori, T., Wang, C., Liu, Y., Nagasako, M., Ruan, J., . . . Liu, X. (2016). A jumping shape memory alloy under heat. *Scientific Reports*, 6(1), 1-6.
8. Yang, J., Wang, Q., Yin, F., Cui, C., Ji, P., & Li, B. (2016). Effects of grain refinement on the structure and properties of a CuAlMn shape memory alloy. *Materials Science and Engineering: A*, 664, 215-220.
9. Dasgupta, R. (2014). A look into Cu-based shape memory alloys: Present scenario and future prospects. *Journal of Materials Research*, 29(16), 1681.
10. Canbay, C. A., Karaduman, O., Ünlü, N., Baiz, S. A., & Özkul, İ. (2019). Heat treatment and quenching media effects on the thermodynamical, thermoelastical and structural characteristics of a new Cu-based quaternary shape memory alloy. *Composites Part B: Engineering*, 174, 106940.
11. Karaduman, O., Canbay, C. A., Özkul, İ., Baiz, S. A., & Ünlü, N. (2018). Production and characterization of ternary Heusler shape memory alloy with A new composition. *JOURNAL OF MATERIALS AND ELECTRONIC DEVICES*, 1(1), 16-19.
12. Karaduman, O., Canbay, C. A., Ünlü, N., & Özkul, İ. (2019). *Analysis of a newly composed Cu-Al-Mn SMA showing acute SME characteristics*. Paper presented at the AIP Conference Proceedings.
13. Tong, H., & Wayman, C. (1974). Characteristic temperatures and other properties of thermoelastic martensites. *Acta Metallurgica*, 22(7), 887-896.
14. Canbay, C. A., Karaduman, O., Özkul, I., & Ünlü, N. (2020). Modifying Thermal and Structural Characteristics of CuAlFeMn Shape Memory Alloy and a Hypothetical Analysis to Optimize Surface-Diffusion Annealing Temperature. *Journal of Materials Engineering and Performance*, 29(12), 7993-8005.
15. Prado, M., Decorte, P., & Lovey, F. (1995). Martensitic transformation in Cu-Mn-Al alloys. *Scripta metallurgica et materialia*, 33(6).
16. Ahlers, M. (1995). Phase stability of martensitic structures. *Le Journal de Physique IV*, 5(C8), C8-71-C78-80.
17. Braga, F. d. O., Matlakhov, A. N., Matlakhova, L. A., Monteiro, S. N., & Araújo, C. J. d. (2017). Martensitic transformation under compression of a plasma processed polycrystalline shape memory CuAlNi alloy. *Materials Research*, 20(6), 1579-1592.
18. Wee, Y., Abubakar, T., Hamzah, E., & Saud, S. N. (2015). Phase transformation and microstructure behaviour of Cu-Al-Ni shape memory alloys incorporated with cobalt addition. *Jurnal Teknologi*, 74(10).
19. Saud, S. N., Hamzah, E., Abubakar, T., & Bakhsheshi-Rad, H. (2015). Thermal aging behavior in Cu-Al-Ni-xCo shape memory alloys. *Journal of Thermal Analysis and Calorimetry*, 119(2), 1273-1284.
20. Canbay, C. A., Karaduman, O., & Özkul, İ. (2019). Investigation of varied quenching media effects on the thermodynamical and structural features of a thermally aged CuAlFeMn HTSMA. *Physica B: Condensed Matter*, 557, 117-125.
21. Yang, S., Su, Y., Wang, C., & Liu, X. (2014). Microstructure and properties of Cu-Al-Fe high-temperature shape memory alloys. *Materials Science and Engineering: B*, 185, 67-73.
22. Yang, S., Zhang, F., Wu, J., Zhang, J., Wang, C., & Liu, X. (2017). Microstructure characterization, stress-strain behavior, superelasticity and shape memory effect of Cu-Al-Mn-Cr shape memory alloys. *Journal of materials science*, 52(10), 5917-5927.
23. Karthick, S., & Palani, I. (2019). Design and development of Cu-Al-Mn shape memory alloy coated optic fiber sensor and its actuation characteristics for condition monitoring of structures. *ISSS Journal of Micro and Smart Systems*, 8(2), 89-99.



© Author(s) 2021. This work is distributed under <https://creativecommons.org/licenses/by-sa/4.0/>



## Influence of the effect of the ball burnishing process applied to Al 7075-T6 alloy in different nano-aluminum powder-added grease environment on surface quality

Süleyman Cinar Cagan<sup>\*1</sup>, Berat Baris Buldum<sup>1</sup>

<sup>1</sup>Mersin University, Engineering Faculty, Department of Mechanical Engineering, Mersin, Türkiye, [cinarcagan@mersin.edu.tr](mailto:cinarcagan@mersin.edu.tr); [barisbuldum@mersin.edu.tr](mailto:barisbuldum@mersin.edu.tr)

Cite this study: Cagan, S. C., & Buldum, B. B. (2021). Influence of the effect of the ball burnishing process applied to Al 7075-T6 alloy in different nano-aluminum powder-added grease environment on surface quality. *Advanced Engineering Science*, 1, 20-25.

### Keywords

Ball burnishing  
Al 7075  
Surface roughness  
Nanopowder

### Research Article

Received:04.05.2021  
Revised: 01.07.2021  
Accepted:07.07.2021  
Published:15.08.2021



### Abstract

Surface roughness is a very important factor in determining the quality of the product to be obtained, as it affects the production cost and performance of mechanical parts. Surface quality is considered primarily as a design parameter for determining functional properties such as corrosion resistance and fatigue strength of the part. Therefore, this study aims to improve the surface roughness of Al 7075-T6 material, which is generally used in aerospace and defense industries. In addition, Al 7075-T6 alloy is an aluminum alloy used in parts that require high strength in the military and aircraft industry, automotive industry, and nuclear applications. To increase the surface quality of the parts, a ball burnishing apparatus was designed and experiments were carried out by determining four different force parameters. At the same time, the forces were completed in environments where different ratios (0, 1, 3, 5, and 10% by weight) of nano-Al powders were added to the grease. Thanks to these powders, it is aimed to increase the quality of the surface of the ball burnishing Al 7075-T6 alloy. Ball burnishing is a simple, fast, and inexpensive surface improvement process that is used to remove irregularities on the surfaces of materials after processing. This method is a known method of mechanical surface treatment to impart certain physical, mechanical, and tribological properties to the workpiece. This process is based on the principle of burnishing the workpiece with an apparatus to remove the irregularities on the surface by plastic deformation. As a result of the experiment, the effect of each parameter on the surface quality of the Al-7075-T6 alloy was investigated. Thus, the most suitable test parameters affecting the surface quality of Al-7075-T6 alloy were determined.

## 1. Introduction

Aluminum and its alloys are widely used in industry due to their lightweight, strength, and easy forming capabilities [1-3]. Aluminum alloys play an important role in the development of aviation, space, automotive, military, and defense industries due to their lightweight (density 2.81 g/cm<sup>3</sup>) as well as their mechanical properties [4-6]. Among these alloys, the importance and application areas of 7075-T6 quality aluminum alloys are increasing, especially in the defense and aerospace industry [7].

Surface roughness is important in determining the quality of the product to be obtained, as it affects the mechanical properties, performance, and production cost of mechanical parts [8, 9]. Characteristic irregularities occur on the surface of the workpiece after many machining operations [10]. Ball burnishing is a simple, fast, and inexpensive process used to eliminate these irregularities [11]. This process is a well-known mechanical surface treatment method to give the workpiece certain physical, mechanical and tribological properties [12]. This process is based on the principle of compressing by applying an apparatus to obtain a smooth surface by removing

irregularities on the surface by plastic deformation [13]. As a result, this process involves turning, milling, honing, grinding, etc. It can be used in place of other traditional surface treatment techniques.

The parameters affecting the surface quality of the workpiece when the ball burnishing process is applied are workpiece materials, ball materials, ball types, burnishing forces, number of passes, physical properties of the ball (hardness, ball size, etc.), lubricants, feed rates and burnishing speed. When the literature is searched, it is seen that the researchers studied different materials and burnishing process parameters (force, speed, passes, etc.) [14-20]. Studies on the application of ball burnishing under different environmental conditions are limited in the literature, and it is still an issue that needs to be developed. This experimental study aims to obtain optimum surface roughness values of aluminum alloy (Al7075-T6) in different burnishing forces and burnishing environments.

## 2. Method

The experiments were carried out using the Al 7075-T6 aluminum solid bar. The chemical content of Al 7075-T6 used as a workpiece is shown in Table 1. The dimensions of this workpiece material are Ø50 x 280 mm and a total of twenty tests have been carried out using two of them. Each workpiece is divided into ten equal parts. Different parameters have been applied to each part.

**Table 1.** Chemical content (wt.%) of Al 7075-T6 aluminum alloy

Workpiece	Al	Cu	Fe	Mg	Si	Mn	Ti	Zn	Cr
Al7075-T6	Balance	1.94	0.45	2.71	0.37	0.25	0.19	5.63	0.21

The experiments were carried out on a conventional lathe as shown in Figure 1. The Al 7075-T6 workpiece was first turned at 400 rpm to make the surface suitable for testing, and then the surface roughness value was measured. The surface roughness value (Ra) obtained without any processing is 1.558 µm. The experiments were done with a conventional lathe. In addition, using a force gauge, the force parameter used for ball burnishing was accurately determined (Figure 1). The force meter is calibrated every three months. Particle penetration between the ball burnishing apparatus and the contact surface is prevented. This is because anything entering between the interface between the apparatus and the sample adversely affects the quality of the surface. While planning the experimental design, twenty tests were conducted using four different burnishing forces (50, 100, 150, 200N) and five different environments (pure Al, grease with 1%, 3%, 5%, and 10% nano-Al powder additive) (Table 2). 1, 3, 5 and 10 wt % Al powders of nano-size were added into the grease and mixed (Figure 2).

Surface roughness is used as a measure in determining the surface texture of the material [1]. After any test procedure applied to the workpiece, changes in the surface topography of the material occur at the micron level [21]. Determining these changes is very important in terms of the mechanical properties of the part. Since surface roughness helps to determine the performance of any mechanical component with strategic definition, it provides the opportunity to predict the irregularities that may occur on the surface (the formation of cracks or the onset of corrosion) [22]. The surface roughness value is usually calculated by considering the arithmetic mean of absolute values (Ra). According to Figure 2, the Ra value can be expressed by the Equation 1 [23]:

$$Ra = \frac{1}{L} \int_0^L |Y(x)| dx \quad (1)$$

## 3. Results and Discussion

The surface roughness values obtained after the Al 7075-T6 aluminum alloy is ball-burnished in different parameters (Force and Al additive ratio) are given in Table 2. When the quality of the surface where the ball burnishing process is not applied and the quality of the applied surfaces are compared, it is seen that the ball burnishing process improves the surface quality.

The graph of the surface roughness changes according to different % nano-Al powder additive ratios and force parameters is shown in Figure 4. When the graphic is interpreted; although it is observed that the surface roughness value decreases as the percentage of Al additive added to the grease and the force values increase, it is observed that the effect of the % nano-Al powder additive ratio on the surface roughness is more than the force values. Because of the 50 N force value and the 10% nano-Al powder additive rate, the surface roughness value is the lowest.

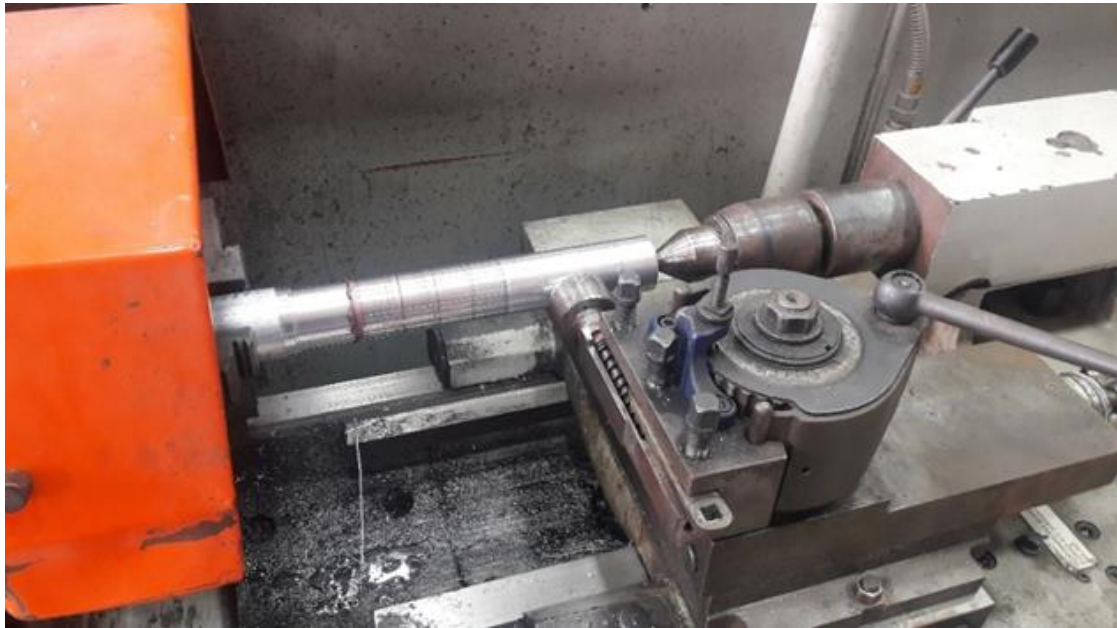


Figure 1. Experimental setup

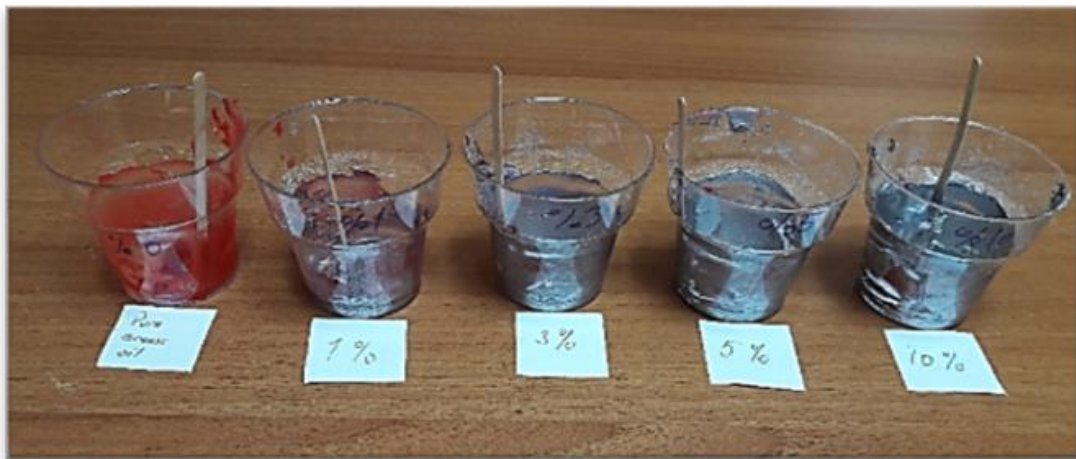


Figure 2. Grease environments with different ratios of nano-Al additive.

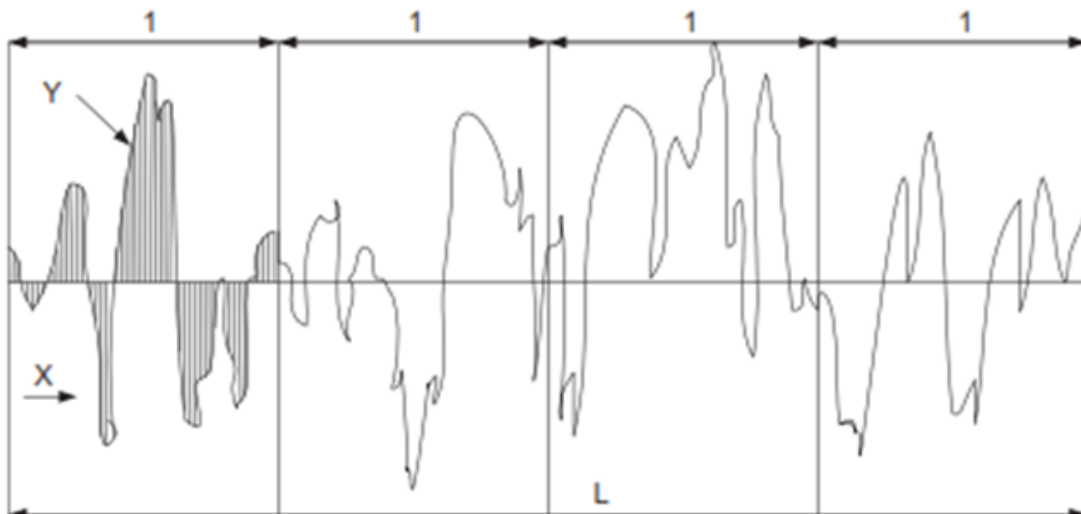
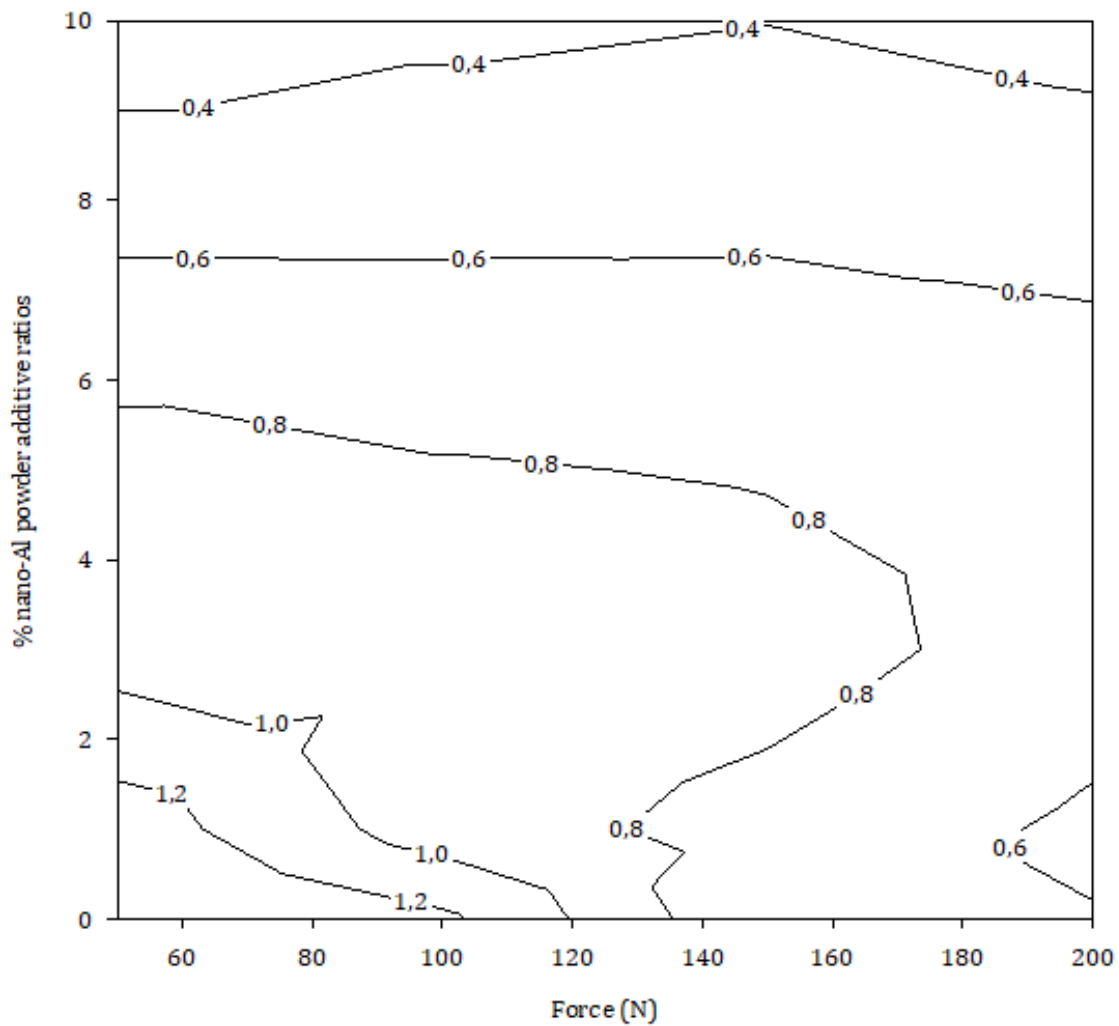


Figure 3. Profile of surface texture [23]

**Table 2.** Experimental parameters and surface roughness results

Experiment number	Force (N)	Environments (%nano-Al powder additive ratio)	Surface Roughness results ( $\mu\text{m}$ )	
			Ra	Rz
1	50	Pure	1,372	5,300
2	50	% 1	1,309	4,949
3	50	% 3	0,907	5,137
4	50	% 5	0,886	4,369
5	50	% 10	0,279	1,591
6	100	Pure	1,239	4,756
7	100	% 1	0,895	4,243
8	100	% 3	0,954	5,434
9	100	% 5	0,816	3,887
10	100	% 10	0,356	1,788
11	150	Pure	0,621	2,706
12	150	% 1	0,727	3,271
13	150	% 3	0,890	5,080
14	150	% 5	0,785	3,146
15	150	% 10	0,396	2,129
16	200	Pure	0,609	3,026
17	200	% 1	0,565	2,998
18	200	% 3	0,698	3,721
19	200	% 5	0,760	3,612
20	200	% 10	0,332	1,921



**Figure 4.** Variation of surface roughness according to different % nano-Al powder additive ratios and force parameters.

#### 4. Conclusion

In this article, a study was conducted on the improvement of the Al 7075-T6 workpiece surface by mechanical methods. The experiments were carried out using the ball burnishing process, one of the mechanical surface improvement processes. In this study, when the effect of different parameters (force and % nano-Al powder additive ratio) on surface quality is examined, the following results are obtained:

- It has been observed that the best results among the measured surface roughness values were obtained in the environment of 50N and 10% nano-Al powder added grease.
- It is concluded that the increase in the contribution ratio and the force separately increases the surface quality.
- The surface roughness value of the Al 7075-T6 workpiece, which is not ball burnished, was 1.558  $\mu\text{m}$ , and the surface roughness value was reduced to 0.279  $\mu\text{m}$  after the ball burnishing process.

#### Funding

This research received no external funding.

#### Author contributions

**Suleyman Cinar Cagan:** Conceptualization, Methodology, Software, Visualization, Investigation **Berat Baris Buldum:** Data curation, Writing-Original draft preparation, Software, Validation, Writing-Reviewing and Editing.

#### Conflicts of interest

The authors declare no conflicts of interest.

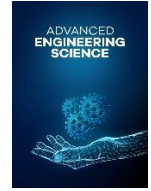
#### References

1. He, C., Zong, W., & Zhang, J. (2018). Influencing factors and theoretical modeling methods of surface roughness in turning process: State-of-the-art. *International Journal of Machine Tools and Manufacture*, 129, 15-26.
2. Del Sol, I., Rivero, A., & Gamez, A. J. (2019). Effects of machining parameters on the quality in machining of aluminium alloys thin plates. *Metals*, 9(9), 927.
3. Cagan, S. C., & Buldum, B. B. (2019). Effects of ball burnishing on the surface quality of Al 7075 alloy. *Materials Testing*, 61(11), 1105-1108.
4. Kuram, E., Ozcelik, B., Huseyin Cetin, M., Demirbas, E., & Askin, S. (2013). Effects of blended vegetable-based cutting fluids with extreme pressure on tool wear and force components in turning of Al 7075-T6. *Lubrication Science*, 25(1), 39-52.
5. Gupta, M. K., Mia, M., Singh, G., Pimenov, D. Y., Sarikaya, M., & Sharma, V. S. (2019). Hybrid cooling-lubrication strategies to improve surface topography and tool wear in sustainable turning of Al 7075-T6 alloy. *The International Journal of Advanced Manufacturing Technology*, 101(1), 55-69.
6. Santos, M. C., Machado, A. R., Sales, W. F., Barrozo, M. A., & Ezugwu, E. O. (2016). Machining of aluminum alloys: a review. *The International Journal of Advanced Manufacturing Technology*, 86(9), 3067-3080.
7. Aamir, M., Giasin, K., Tolouei-Rad, M., & Vafadar, A. (2020). A review: Drilling performance and hole quality of aluminium alloys for aerospace applications. *Journal of Materials Research and Technology*, 9(6), 12484-12500.
8. Buldum, B., & Cagan, S. (2018). Study of ball burnishing process on the surface roughness and microhardness of AZ91D alloy. *Experimental Techniques*, 42(2), 233-241.
9. Saldaña-Robles, A., Plascencia-Mora, H., Aguilera-Gómez, E., Saldaña-Robles, A., Marquez-Herrera, A., & Diosdado-De la Peña, J. A. (2018). Influence of ball-burnishing on roughness, hardness and corrosion resistance of AISI 1045 steel. *Surface and Coatings Technology*, 339, 191-198.
10. Maximov, J., Anchev, A., Duncheva, G., Ganey, N., & Selimov, K. (2017). Influence of the process parameters on the surface roughness, micro-hardness, and residual stresses in slide burnishing of high-strength aluminum alloys. *Journal of the Brazilian Society of Mechanical Sciences and Engineering*, 39(8), 3067-3078.
11. Revankar, G. D., Shetty, R., Rao, S. S., & Gaitonde, V. N. (2014). Analysis of surface roughness and hardness in ball burnishing of titanium alloy. *Measurement*, 58, 256-268.
12. Balland, P., Tabourot, L., Degre, F., & Moreau, V. (2013). Mechanics of the burnishing process. *Precision Engineering*, 37(1), 129-134.

13. García-Granada, A. A., Gomez-Gras, G., Jerez-Mesa, R., Travieso-Rodriguez, J. A., & Reyes, G. (2017). Ball-burnishing effect on deep residual stress on AISI 1038 and AA2017-T4. *Materials and Manufacturing Processes*, 32(11), 1279-1289.
14. Swirad, S., & Wdowik, R. (2019). Determining the effect of ball burnishing parameters on surface roughness using the Taguchi method. *Procedia Manufacturing*, 34, 287-292.
15. Jerez-Mesa, R., Travieso-Rodríguez, J. A., Landon, Y., Dessein, G., Lluma-Fuentes, J., & Wagner, V. (2019). Comprehensive analysis of surface integrity modification of ball-end milled Ti-6Al-4V surfaces through vibration-assisted ball burnishing. *Journal of materials processing technology*, 267, 230-240.
16. Kovács, Z. F., Viharos, Z. J., & Kodácsy, J. (2020). Surface flatness and roughness evolution after magnetic assisted ball burnishing of magnetizable and non-magnetizable materials. *Measurement*, 158, 107750.
17. Uddin, M. S., Hall, C., Hooper, R., Charrault, E., Murphy, P., & Santos, V. (2018). Finite element analysis of surface integrity in deep ball-burnishing of a biodegradable AZ31B Mg alloy. *Metals*, 8(2), 136.
18. Dzionk, S., Scibiorski, B., & Przybylski, W. (2019). Surface Texture Analysis of Hardened Shafts after Ceramic Ball Burnishing. *Materials*, 12(2), 204.
19. Gomez-Gras, G., Travieso-Rodríguez, J. A., González-Rojas, H. A., Nápoles-Alberro, A., Carrillo, F. J., & Dessein, G. (2015). Study of a ball-burnishing vibration-assisted process. *Proceedings of the Institution of Mechanical Engineers, Part B: Journal of Engineering Manufacture*, 229(1), 172-177.
20. Bourebia, M., Laouar, L., Hamadache, H., & Dominiak, S. (2017). Improvement of surface finish by ball burnishing: approach by fractal dimension. *Surface engineering*, 33(4), 255-262.
21. Du, F., He, L., Huang, H., Zhou, T., & Wu, J. (2020). Analysis and Multi-Objective Optimization for Reducing Energy Consumption and Improving Surface Quality during Dry Machining of 304 Stainless Steel. *Materials*, 13(21), 4693.
22. Cagan, S. C., Pruncu, C. I., & Buldum, B. B. (2020). An investigation into ball burnishing process of magnesium alloy on CNC lathe using different environments. *Journal of Magnesium and Alloys*, 8(4), 1061-1070.
23. Zhang, S., To, S., Wang, S., & Zhu, Z. (2015). A review of surface roughness generation in ultra-precision machining. *International Journal of Machine Tools and Manufacture*, 91, 76-95.



© Author(s) 2021. This work is distributed under <https://creativecommons.org/licenses/by-sa/4.0/>



## Shape memory effect characterization of a ternary CuAlNi high temperature SMA ribbons produced by melt spinning method

Oktaý Karaduman<sup>\*1</sup>, İskender Özkul<sup>2</sup>, Canan Aksu Canbay<sup>1</sup>

<sup>1</sup> Firat University, Faculty of Science, Department of Physics, Elazığ, Türkiye, [okinist@hotmail.com](mailto:okinist@hotmail.com); [caksu@firat.edu.tr](mailto:caksu@firat.edu.tr)

<sup>2</sup> Mersin University, Faculty of Engineering, Department of Mechanical Engineering, Mersin, Türkiye, [iskender@mersin.edu.tr](mailto:iskender@mersin.edu.tr)

Cite this study: Karaduman, O., Özkul, İ., & Canbay, A. C. (2021). Shape memory effect characterization of a ternary CuAlNi high temperature SMA ribbons produced by melt spinning method. *Advanced Engineering Science*, 1, 26-33.

### Keywords

CuAlNi HTSMA ribbon  
Shape memory effect  
Martensite  
Shape recovery ratio  
DSC  
DTA  
X-ray diffraction

### Research Article

Received:03.05.2021  
Revised: 01.07.2021  
Accepted:06.07.2021  
Published:15.08.2021



### Abstract

In this study, the shape memory effect characteristics of a ternary CuAlNi shape memory alloy (HTSMA) ribbons produced by melt spinning method was investigated by performing thermal and structural measurements. To investigate shape memory effect properties of the alloy ribbon some isothermal calorimetry, structural and shape recovery ratio tests were performed. The differential scanning calorimetry (DSC) test result showed the peaks of the reversible martensitic phase transformations occurred in a high temperature region (in between  $\sim 192^{\circ}\text{C}$  -  $293^{\circ}\text{C}$ ) during the heating and cooling processes of the CuAlNi alloy ribbon. The hysteresis gap of the ribbon alloy was found narrow ( $20.77^{\circ}\text{C}$ ). Some other related thermodynamical parameters parameters of the alloy were determined, too. The differential thermal analysis (DTA) measurement taken from room temperature to  $900^{\circ}\text{C}$  revealed the sequenced multiple solid solid phase transitions in the high temperature  $\beta$ -phase region and this was found as compatible with the common behavior of the Cu-rich alloys. Theoretical pre-assesment on the martensite phases of the alloy was deduced from the calculated average valence electron concentration (e/a) value (1.54) of the alloy and this was proved by structural XRD test performed also in room conditions. The X-ray diffraction pattern of the alloy revealed the presence of the volumetrically dominant  $\gamma 1'$  martensite phase over the collateral secondary  $\beta 1'$  martensite phase in the alloy. A shape recovery performance test upon thermomechanical bending was performed on the alloy, too.

## 1. Introduction

Shape memory alloy (SMA) ribbons are extensively demanded due to the useful functionalities of such miniaturized SMAs in the related integrated micro-controllers and micro-electro-mechanical systems (MEMS) applications such as microactuators, microgrippers, microvalves etc. [1, 2]. Melt spinning (Figure 1) is an easy manufacturing method and by this method very thin columnar SMA ribbons with very small grain sizes can be directly obtained even without doing a further heat-treatment homogenization and quenching (rapid cooling) processes [2, 3]. Moreover, by this manufacturing method the maximal reversible strain in longitudinal direction can be increased, too [4].

The low-cost Cu-based SMAs are generally regarded as the best alternative to the most commercial NiTi SMAs with superior shape memory alloy properties but much higher costs. Plus, Cu-based SMAs have high transformation temperatures, better thermal and electrical conductivity, and also large recoverable strain [5]. As concerning to find alternative SMAs with high transformation temperatures (above  $100^{\circ}\text{C}$ ) or named as high

temperature SMAs (HTSMAs), the CuAlNi SMAs are seen the best option among the other Cu-based SMAs due to their high thermal stability [3, 4]. But the polycrystalline CuAlNi SMAs exhibit poor mechanical properties due to their brittleness caused from large grain sizes. Producing CuAlNi alloys in ribbon forms by melt spinning method is established one of the ways for grain refinement.

The transformation temperatures of SMAs are ultimately sensitive to chemical composition, even very small differences in alloying compositions can enormously change the transformation temperatures. Hence, transformation temperatures demanded in various SMA (and HTSMA) applications can be regulated by tuning alloy composition.

In this work, the ternary CuAlNi HTSMA ribbons were manufactured by melt spinning method. Without doing any further heat-treatment and quenching procedures on the ribbon alloy, the shape memory effect characterization was made by thermostructural DSC, DTA and XRD tests and thermo-mechanical shape recovery performance test on the alloy ribbon was also carried out.

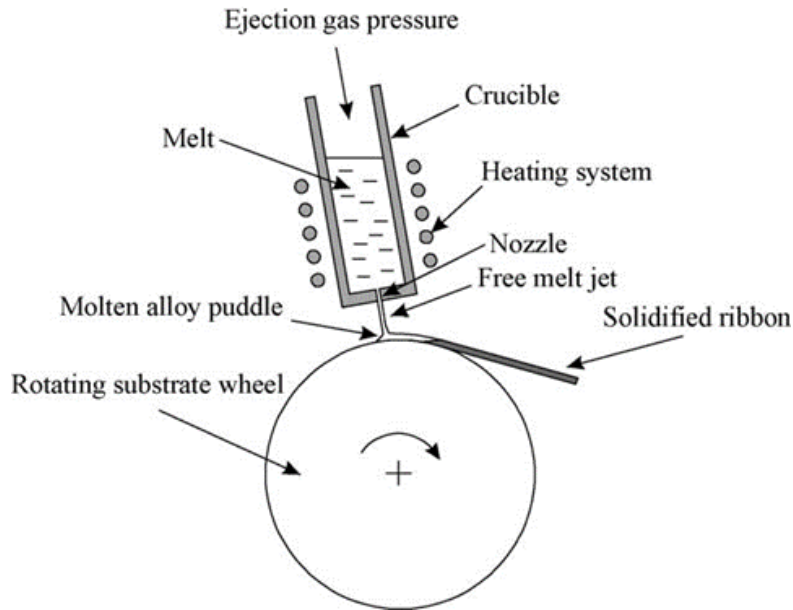


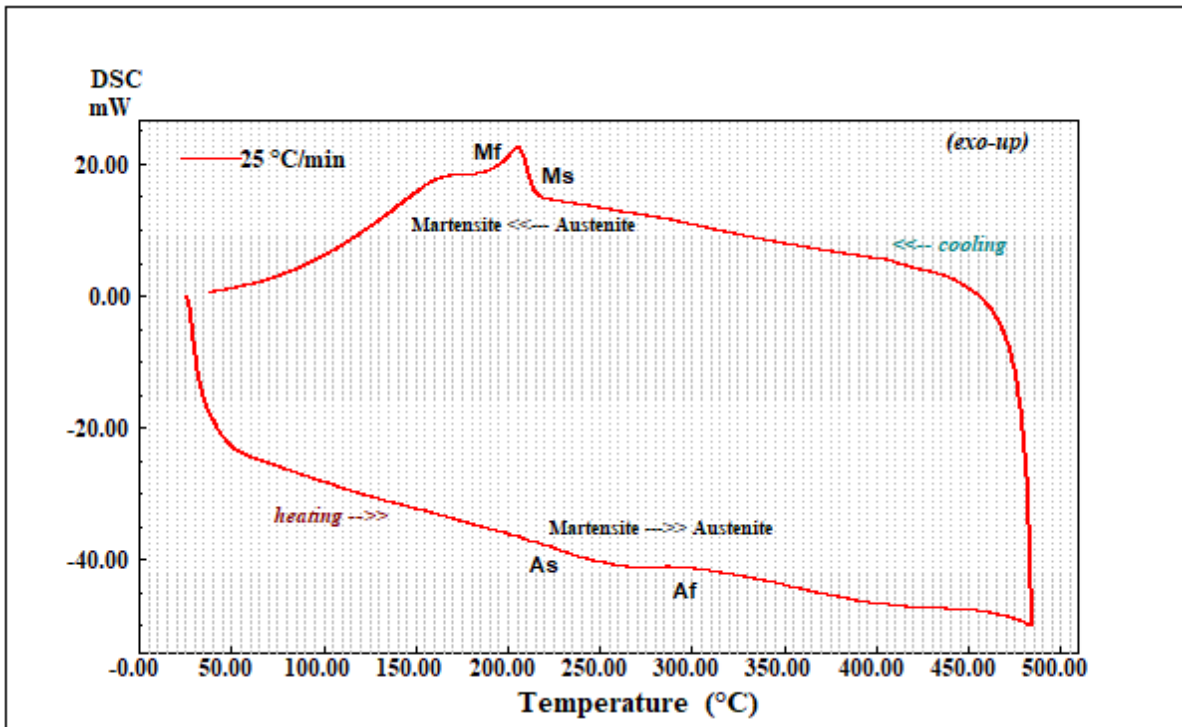
**Figure 1.** Schematic illustration of a free jet melt spinner [3]

## 2. Method

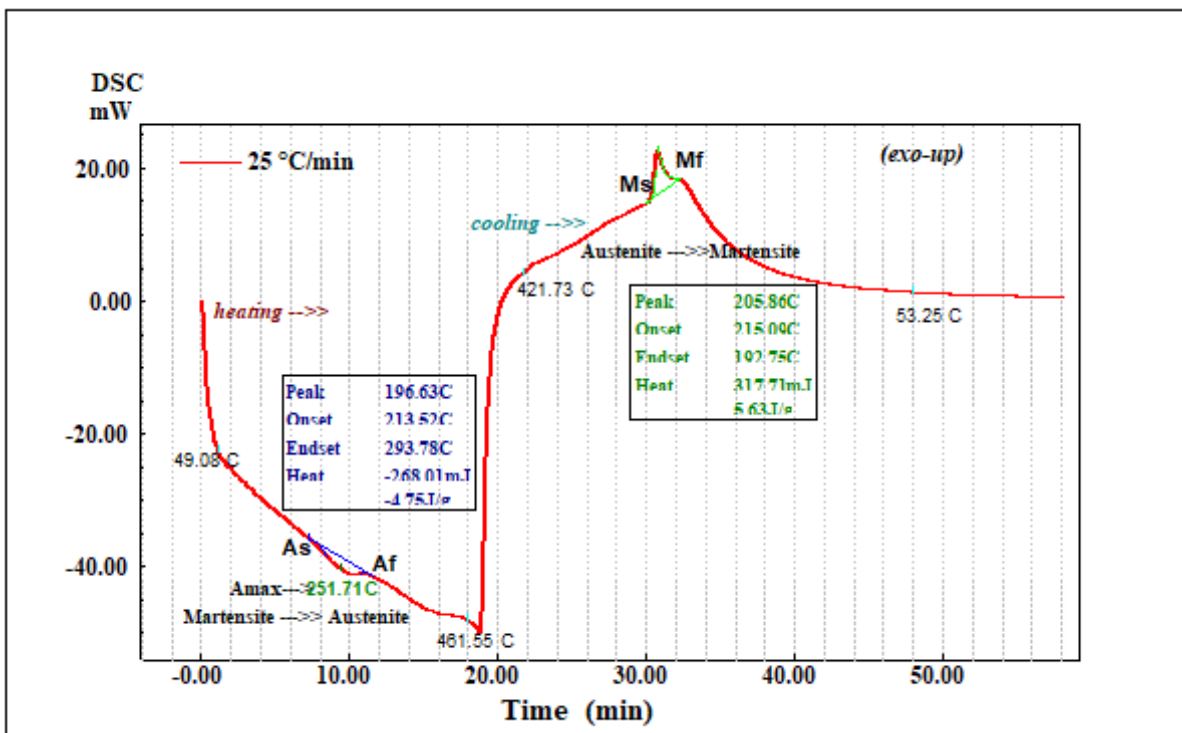
The CuAlNi SMA ribbons with a new alloy composition of 71.08Cu-25.04Al-3.88Ni (at%) or 82.5Cu-12.34Al-4.16Ni (wt%) were fabricated by melt spinning method. In this process, at first, the powders of the alloying Cu, Al, and Ni elements with high purity (%99.99) were mixed and then the pellet forms of this powder mixture were obtained by applying pressure. Then the pellets were melted via melt spinning procedure by using an Edmund Buehler melt spinner system in argon atmosphere to prevent oxidation of alloy ribbons. Thus, the CuAlNi alloy ribbons with 15  $\mu\text{m}$  thickness and  $\sim 5$  mm width was successfully produced. The test specimens of the obtained melt spun alloy ribbons were prepared by cutting them properly for the measurements. A Shimadzu 60A label DSC instrument was utilized for performing the DSC test taken at a single heating/cooling rate of 25  $^{\circ}\text{C}/\text{min}$  under 100 ml/min constant argon gas flow. Under same gas flow and also at a single 25  $^{\circ}\text{C}/\text{min}$  of heating/cooling rate, the cyclical DTA test was carried out by using a Shimadzu DTG-60AH system in between room temperature and 900  $^{\circ}\text{C}$ . The shape recovery performance test of the alloy ribbon upon bending load was performed and the shape recovery ratio between the deformed martensitic shape (storage state, S) of ribbon and the recovered austenitic shape (recovery state, R) formed by applied heat on the deformed ribbon was calculated by using the determined position angles of two shape states. The alloy composition was detected by a Zeiss Evo MA10 model EDX equipment under room conditions. By using  $\text{CuK}\alpha$  radiation the X-ray diffraction (XRD) test made at room temperature by using a Rigaku RadB-DMAX II diffractometer displayed the diffraction peaks planes reflected from the atomic crystal planes of the martensite structures at room temperature.

## 3. Results

The thermocyclical DSC test result of the CuAlNi ribbon obtained at a single heating/cooling rate of 25  $^{\circ}\text{C}/\text{min}$  is given as graphic of DSC heat flow (mW) versus temperature ( $^{\circ}\text{C}$ ) axis in Figure 2-a, and the same graphic drawn out on time axis in Figure 2-b. As seen on the both version of the DSC graphic, the correspondent up-exo (on cooling) and down-endo (on heating) peaks observed at between  $\sim 192$   $^{\circ}\text{C}$  and  $\sim 293$   $^{\circ}\text{C}$  indicates the backward austenite to martensite (A $\rightarrow$ M) and forward martensite to austenite (M $\rightarrow$ A) phase transformations, respectively.



(a)



(b)

**Figure 2.** The DSC test result of the produced CuAlNi SMA ribbon; a) the DSC heating/cooling curve (thermogram) cycled on temperature axis, b) the same DSC curve drawn out on time axis and with data insets of the analysed forward and backward martensitic transformation peaks. In these peak analysis data insets, which were automatically inserted by DSC analyser program applying tangent method on the selected area of a peak, the onset temperatures are the phase start temperatures ( $A_s$  and  $M_s$ ), the endset temperatures are phase finish temperatures ( $A_f$  and  $M_f$ ) and the enthalpy change values (J/g) as integral of transformation peak areas were also directly given at the bottom of these data insets.

For this reversible martensitic transformation, the characteristic phase start and finish temperatures ( $A_s$ ,  $A_f$ ,  $M_s$ , and  $M_f$ ), the maximum temperature  $M \rightarrow A$  peak ( $A_{max}$ ) (actually here this is the minimum in the case of endo-peaks seen in the tests made by Shimadzu DSC instrument), the hysteresis gap ( $A_s - M_f$ ), the equilibrium temperature ( $T_0$ ), the enthalpy ( $\Delta H_{M \rightarrow A}$ ) and entropy ( $\Delta S_{M \rightarrow A}$ ) change amounts for  $M \rightarrow A$  transformations were obtained and tabulated in [Table 1](#).

**Table 1.** The characteristics martensitic transformation temperatures and some related kinetic parameters of the CuAlNi HTSMA ribbon.

Heating/cooling rate (°C/min)	$A_s$ (°C)	$A_f$ (°C)	$A_{max}$ (°C)	$M_s$ (°C)	$M_f$ (°C)	$A_s - M_f$ (°C)	$T_0$ (°C)	$\Delta H_{M \rightarrow A}$ (J/g)	$\Delta S_{M \rightarrow A}$ (J/g°C)
25	213.52	293.78	251.71	215.09	192.75	20.77	254.44	4.75	0.01867

Apart from the DSC result, an empirical formula ([Equation 1](#)) [4] is given for making an estimation of the  $M_s$  temperature of CuAlNi alloys;

$$M_s(°C) = 2020 - [134 \times (wt.\%Al)] - [45 \times (wt.\%Ni)] \quad (1)$$

By substituting the mass percentage (wt.%) values of Al and Ni alloying elements in the [Equation 1](#), the  $M_s$  temperature of the produced CuAlNi HTSMA ribbon was found as 179.24 °C and this value was found close to the  $M_s$  value (215.09 °C) determined by DSC analysis (given in [Table 1](#)). The reason of the difference between these two  $M_s$  values may be caused from the DSC test and the cooling rate or the presence of small local composition diversities in the ribbon alloy (without making post heat treatment and quenching after melt spinning, some hypoeutectical precipitations may be remained in the alloy ribbons, and this is going to be shown in the XRD result section ahead).

The equilibrium temperature ( $T_0$ ) is an important kinetic parameter for SMAs. It is the temperature at where the chemical Gibbs free energy (G) values of two austenite and martensite phases are balanced, meaning that at this temperature there is zero driving force can trigger the alloy to make transform to any one of the two opposite phases [6]. By using  $T_0 = 0.5 \times (A_f + M_s)$  formula [6] the  $T_0$  value of the ribbon alloy was found as given in [Table 1](#). The entropy change ( $\Delta S_{M \rightarrow A}$ ) of the endothermic  $M \rightarrow A$  transformation was found by using  $\Delta S_{M \rightarrow A} = \Delta H_{M \rightarrow A} / T_0$  relation [6, 7].

The DTA cyclic curve of the CuAlNi alloy ribbon obtained at the single running heating/cooling rate of 25 °C/min is presented in Fig.3. According to this figure, on the heating fragment of the DTA curve, the appeared sequential peaks indicated the multiple phase transformations of “**B1**(austenite, L2<sub>1</sub>)→**B2**(metastable)→precipitating( $\alpha + \gamma_2$ )→**euctoid** recomposition (of the precipitates)→**B2**(ordered)→**A2**(disordered)” throughout of the high temperature  $\beta$ -phase region, which is a common behavior of Cu-based alloys. [6, 7].

The average valence electron concentration per atom (e/a) value of Cu-based SMAs can give some pre-knowledge about the formed martensite phases with their volumetric comparison in those alloys. By using  $e/a = \sum f_i v_i$  formula [7], where  $f_i$  is the each atomic fraction (at.%) of the alloying elements and  $v_i$  represents the corresponding valence electron numbers of these elements. This e/a value found higher than 1.49 implies that the hexagonal  $\gamma_1'$ (2H) martensite phase should have dominantly formed in the alloy over monoclinical  $\beta_1'$ (M18R) martensite phase [6, 7]. This theoretical prediction is to be proved by the result of structural X-ray diffraction test performed on the alloy ribbon as given in [Figure 4](#).

The XRD pattern of the alloy ribbon is given in Fig.4. The highest  $\gamma_1'$ (211) martensite peak seen on this X-ray diffraction pattern shows a little dominancy of this martensite phase over the  $\beta_1'$  martensite, and this affirms the prediction made by e/a value of the alloy ribbon. The other observed peaks on the XRD pattern are some other martensite phases of  $\gamma_1'$  and  $\beta_1'$ ,  $\beta_1$ , and precipitates of  $\gamma_1$ ,  $\gamma_2$ , and  $\alpha$ Cu [5, 8-15]. These complex and short peaks including many small precipitation peaks indicate the high polycrystalline nature of the alloy ribbon matrix. This was also caused because of not making a post-heat-treatment after melt spinning process.

The thermomechanical bending test upon loading, unloading and recovering by heat was performed to test the shape memory recovery ratio ( $\eta$ ) value of the ribbon alloy. The images of this test is given in [Figure 5-a](#) and [Figure 5-b](#). A formula [16] to calculate the shape recovery ratio ( $\eta$ ) is given in [Equation 2](#);

$$\eta = \frac{\theta_R}{180 - \theta_e} \times 100 \quad (2)$$

where;  $\theta_e$  is the angle (determined as  $\sim 20^\circ$ , in Figure 5-b) in between loaded bending and unloaded plastically deformed (martensite) shape position, and  $\theta_R$  angle (determined as  $\sim 50^\circ$ , in Figure 5-b) between the unloaded shape position and original shape (R, recovery) position of the alloy ribbon. Thus, the shape recovery ratio ( $\eta$ ) of the melt spun CuAlNi HTSMA ribbon was found as  $\sim 31.25\%$  this value could be enhanced more by optimizing test conditions. Also, the alloy ribbon was tended to fracture very much during the bending process, mostly because of its very small thickness.

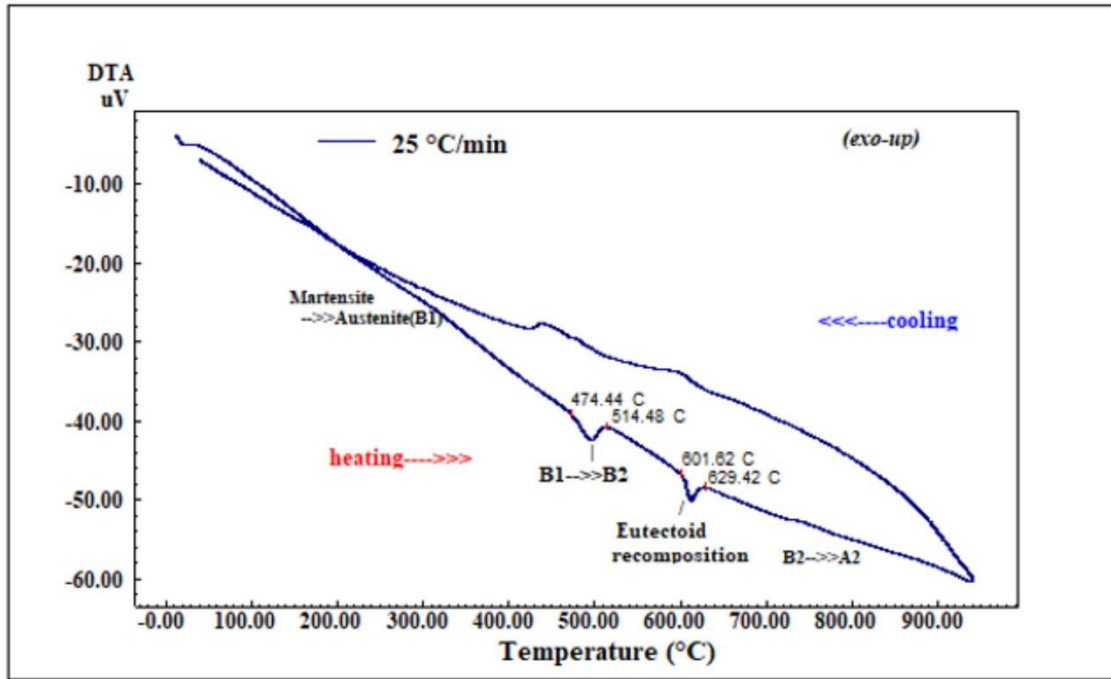


**Figure 3.** The cyclic DTA heating/cooling curve of the CuAlNi SMA ribbon displays the multiple phase transformations of “B1(austenite, L2<sub>1</sub>) → B2(metastable) → precipitating(α+γ<sub>2</sub>) → eutectoid reposition (of the precipitates) → B2(ordered) → A2 (disordered)” throughout of its high temperature β-phase region, which is a common behaviour of Cu-based alloys.

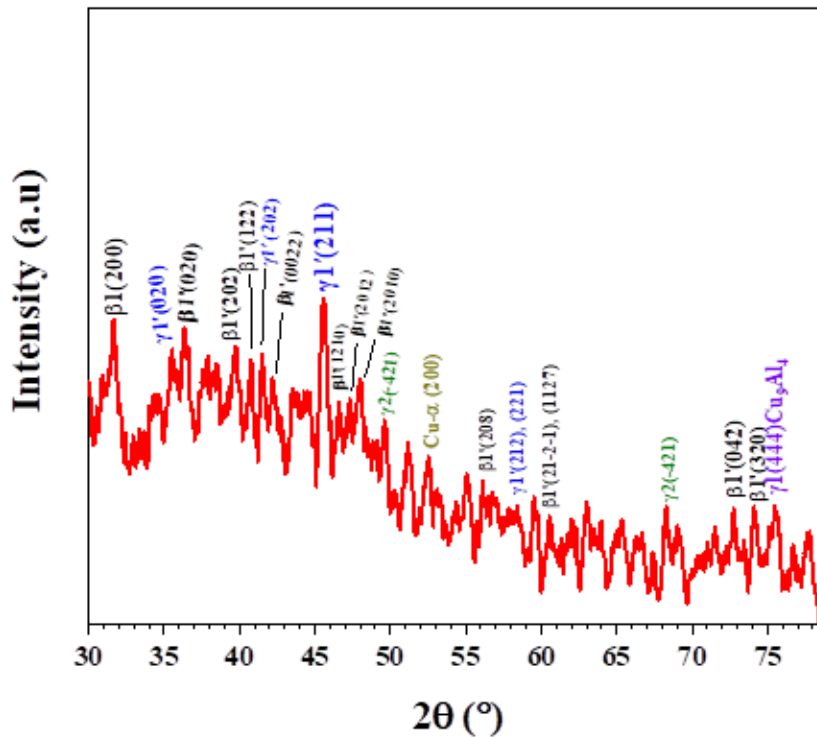


**Figure 4.** The XRD test result of the produced CuAlNi HTSMA ribbon. The main  $\gamma'1'(211)$  martensite peak seen on this X-ray diffraction pattern shows the dominance of this martensite phase over the  $\beta1'$  martensite.

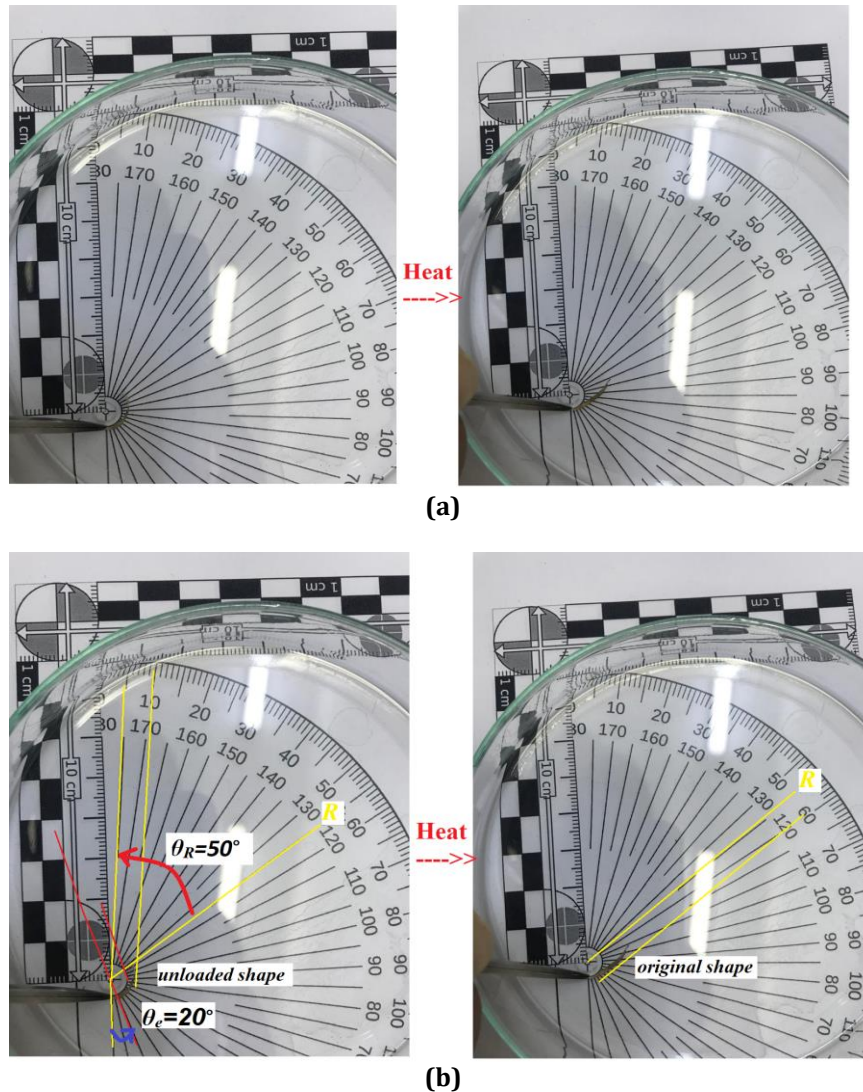


**Figure 5.** The shape recovery performance test of the CuAlNi HTSMA ribbon. a) as pictures of unloaded ribbon in deformed martensite state and after recovery induced by heat, b) same pictures with determined  $\theta_e$  angle between the loaded and unloaded (plastically-deformed) martensite shapes' positions and  $\theta_R$  angle between unloaded shape position and original austenite shape (R, recovery) position.

#### 4. Conclusion

In this work, the CuAlNi HTSMA ribbons with 15 micrometer thickness were successfully manufactured by melt spinning method. The shape memory effect characterization of HTSMA ribbon was implemented by performing thermal DSC/DTA, structural XRD tests, the shape recovery performance of the alloy was tested by making thermo-mechanical bending test. The DSC test showed the alloy ribbon having a shape memory effect property based on the martensitic phase transformation occurred at between  $\sim 192^\circ\text{C}$  and  $\sim 293^\circ\text{C}$  and this range. The DTA test revealed the alloy ribbon's behaviour in high temperature  $\beta$ -phase region as compatible with the common behaviour of the Cu-based alloys. The XRD peaks showed the polycrystalline structure of the alloy including the dominant hexagonal 2H martensite phase in the alloy ribbon at room temperature. The shape recovery ratio of the melt spun CuAlNi HTSMA ribbon tested by thermomechanical bending was found as  $\sim 31.25\%$ , which can be optimized. In conclusion, this melt spun HTSMA ribbon with a new composition may be used in various miniaturized HTSMA applications such as thermo-electro-mechanical systems, microactuators and related applications.

## Acknowledgement

This research work is a part of Ph.D. thesis works of Oktay Karaduman supervised by Assoc. Prof. Dr. Canan Aksu CANBAY at Firat University, Faculty of Science, Department of Physics.

## Funding

This research received no external funding.

## Author contributions

**Oktay Karaduman:** Conceptualization, Methodology, Software **İskender Özkul:** Data curation, Writing-Original draft preparation, Software, Validation. **Canan Aksu Canbay:** Visualization, Investigation, Writing-Reviewing and Editing.

## Conflicts of interest

The authors declare no conflicts of interest.

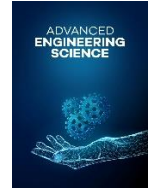
## References

1. Jani, J. M., Leary, M., Subic, A., & Gibson, M. A. (2014). A review of shape memory alloy research, applications and opportunities. *Materials & Design (1980-2015)*, 56, 1078-1113.
2. López Cuellar, E., López Pavón, L., Nuñez Mendoza, E., Araújo, C. J. D., Castro, W. B. D., Gonzalez, C., & Otubo, J. (2016). Effect of spun velocities and composition on the microstructure and transformation temperatures of TiNi shape memory ribbons. *Materials Research*, 19(5), 1132-1137.
3. Font, J., Cesari, E., Muntasell, J., & Pons, J. (2003). Thermomechanical cycling in Cu–Al–Ni-based melt-spun shape-memory ribbons. *Materials Science and Engineering: A*, 354(1-2), 207-211.
4. Lojen, G., Anžel, I., Kneišl, A., Križman, A., Unterweger, E., Kosec, B., & Bizjak, M. (2005). Microstructure of rapidly solidified Cu–Al–Ni shape memory alloy ribbons. *Journal of Materials Processing Technology*, 162, 220-229.
5. Matlakhova, L. A., Pereira, E. C., Pulnev, S. A., Shigue, C. Y., & Palii, N. A. (2020). Physical and Structural Characterization of Monocrystalline Cu-13.7% Al-4.2% Ni alloy submitted to Thermo-Cyclical Treatments under Applied Loads. *Metals*, 10(2), 219.
6. Canbay, C. A., Karaduman, O., Ünlü, N., Baiz, S. A., & Özkul, İ. (2019). Heat treatment and quenching media effects on the thermodynamical, thermoelastical and structural characteristics of a new Cu-based quaternary shape memory alloy. *Composites Part B: Engineering*, 174, 106940.
7. Canbay, C. A., & Karaduman, O. (2021). The photo response properties of shape memory alloy thin film based photodiode. *Journal of Molecular Structure*, 1235, 130263.
8. Braga, F. d. O., Matlakhov, A. N., Matlakhova, L. A., Monteiro, S. N., & Araújo, C. J. d. (2017). Martensitic transformation under compression of a plasma processed polycrystalline shape memory CuAlNi alloy. *Materials Research*, 20(6), 1579-1592.
9. Saud, S. N., Hamzah, E., Abubakar, T., & Bakhsheshi-Rad, H. (2015). Thermal aging behavior in Cu–Al–Ni–xCo shape memory alloys. *Journal of Thermal Analysis and Calorimetry*, 119(2), 1273-1284.
10. Bilican, D., Kurdi, S., Zhu, Y., Solsona, P., Pellicer, E., Barber, Z. H., . . . Fornell, J. (2019). Epitaxial versus polycrystalline shape memory Cu–Al–Ni thin films. *Coatings*, 9(5), 308.
11. Najib, A. S. M., Saud, S. N., & Hamzah, E. (2019). Corrosion Behavior of Cu–Al–Ni–xCo Shape Memory Alloys Coupled with Low-Carbon Steel for Civil Engineering Applications. *Journal of Bio-and Tribo-Corrosion*, 5(2), 47.
12. Zhang, X. & Q.-S. Liu, *Influence of alloying element addition on Cu–Al–Ni high-temperature shape memory alloy without second phase formation*. *Acta Metallurgica Sinica (English Letters)*, 2016. 29(9): p. 884-888.
13. Chentouf, S., Bouabdallah, M., Gachon, J., Patoor, E., & Sari, A. (2009). Microstructural and thermodynamic study of hypoeutectoidal Cu–Al–Ni shape memory alloys. *Journal of Alloys and Compounds*, 470(1-2), 507-514.
14. Canbay, C.A., O. Karaduman, & İ. Özkul, *Investigation of varied quenching media effects on the thermodynamical and structural features of a thermally aged CuAlFeMn HTSMA*. *Physica B: Condensed Matter*, 2019. 557: p. 117-125.

15. Saud, S. N., Hamzah, E., Abubakar, T., & Bakhsheshi-Rad, H. (2015). Thermal aging behavior in Cu–Al–Ni–xCo shape memory alloys. *Journal of Thermal Analysis and Calorimetry*, 119(2), 1273-1284.
16. Jiao, Y., Wen, Y., Li, N., He, J., & Teng, J. (2010). Effect of solution treatment on damping capacity and shape memory effect of a CuAlMn alloy. *Journal of Alloys and Compounds*, 491(1-2), 627-630.



© Author(s) 2021. This work is distributed under <https://creativecommons.org/licenses/by-sa/4.0/>



## Design parameters of sand filtration systems in wastewater treatment process

Ece Kalay <sup>\*1</sup>, Hasan Sarioğlu <sup>1</sup>, İskender Özkul <sup>2</sup>

<sup>1</sup> Ergil Group and Aager GMBH, Research and Development Department, Mersin, Türkiye, eecekalay@gmail.com; hasan.sarioglu@aager.de

<sup>2</sup> Mersin University, Engineering Faculty, Mechanical Engineering Department, Mersin, Türkiye, iskender@mersin.edu.tr

Cite this study: Kalay, E., Sarioğlu, H., & Özkul, İ. (2021). Design parameters of sand filtration systems in wastewater treatment process. *Advanced Engineering Science*, 1, 34-42.

### Keywords

Sand filtration  
Backwashing  
Wastewater treatment  
Filtration hydraulics

### Research Article

Received:06.05.2021  
Revised: 02.07.2021  
Accepted:07.07.2021  
Published:15.08.2021



### Abstract

In parallel with the increasing population of the world, natural water resources are also decreasing day by day. Technologies need to be improved due to the official regulations for the protection of the environment and the increased need for water in enterprises. It is important to minimize the amount of waste water and recover valuable particles. Sand filtration is a system that has been frequently used in waste water recovery processes for years. It is effective in removing large particles, suspended solids and particles such as clay and silt that cause turbidity in water from water. In this study, the basic mechanism and design criteria of the system to obtain the best treatment efficiency in sand filtering systems are examined. However, more research is needed to focus on the composition and properties at the molecular level.

## 1. Introduction

Water scarcity is one of the major problems of many countries in the 21st century. This will be one of the most critical environmental issues in ten years. Southern states of the USA, Southern Europe, North Africa, the Middle East and Australia are already struggling with this problem [1].

The water in the world is 1 billion 400 million km<sup>3</sup> (1 km<sup>3</sup> = 1 billion m<sup>3</sup>). 97.5% of this water consists of salty water in the seas and oceans. The remaining 2.5% is fresh water. A very small part of this ratio is used for various purposes. The percentage of the total amount of water in the world is presented in Table 1 [2]. We should consume these extremely limited natural water resources consciously.

Wastewater has an important water resource potential in places with a high population, in arid regions and in cases where quality water is limited. With water recovery systems, energy consumption and water supply costs can be reduced. In addition, the deterioration of the quality of surface waters can be prevented. As a result, treated water can be reused in various areas. Usage and application areas of treated wastewater are shown in Table 2 [3].

**Table 1.** Percentage of total water in the world

Percentage	%
The amount of salt water in the seas and oceans	97.5
Amount of fresh water	2.5
The amount of water evaporating per year	0.036
The amount of water falling with rainfall per year	0.007
Amount of water flowing with rivers	0.003
Technical and economical amount of water available	0.00064

Water must be brought to certain standards in the reuse of wastewater process. The recovery of water is theoretically possible at any time under suitable conditions. This depends on economic possibilities. The technology to be selected for the reuse of treated water; The properties of treated wastewater should be determined by considering quality criteria for reuse purposes, reliability, ease of operation and economic possibilities [4].

**Table 2.** Usage area and applications of treated wastewater [2]

Reuse	Applications
Environmental applications	bogs and wetlands, parks, lakes, fishing and aquaculture, stream flow regulation
Agriculture and garden irrigation	feed and seed products, feed water, grass and forests, nursery garden
Underground water discharge	Providing control for salt water inlet
Urban applications	Fire protection, Street / car washing, air conditioning, toilet flushing
Industrial applications	Cooling, boiler feeding, Construction, Flue gas cleaning
For drinking purposes	Direct drinking, indirect drinking

Reverse osmosis (RO) has effective results in desalination processes. Oron et al. [5] initially treated 81% of wastewater with an electrical conductivity of 2020  $\mu\text{S}/\text{cm}$ . In their other study, they increased the  $\text{Na}^+$  concentration of 208 mg/L by 83%. In addition, they were able to remove the initial Cl concentration of 48 mg / L by 80% reverse osmosis. Reverse osmosis can remove sodium ions and divalent cations. Therefore, it is very effective in reducing sodium adsorption rate [5].

Yim et al. [6], have achieved virus removal from wastewater at a rate of 99% using ultrafiltration technology.

Hyun et al. [7], results provided a 95% removal efficiency for heavy metals such as Fe, Mn, Cu, Cr and Pb under optimal operating conditions after a series of biofiltration and membranes. It is concluded that treated water is suitable for use in agricultural areas. Agricultural irrigation and ultraviolet system (FTS) are also suitable for reuse of wastewater. The results of the research showed that it can remove 76% of As, 80% of Cd and Cu, 88% of Cr and Pb, 97% of Zn.

Nakada et al. [8] examined the removal of endocrine disrupting chemicals with 24 drugs and personal care products in the secondary wastewater of the sewage treatment plant with sand filtration and ozonation and found that the removal of most pollutants was more than 80%.

In this study, the basic mechanism and design criteria to achieve the best treatment efficiency in sand filtration systems varying according to operating conditions were examined.

## 2. Filtration mechanism

The waters that are subjected to the filtration process are high quality exit waters. During this process, the quality of water increases with the retention of suspended and colloid materials, removal of microorganisms and changes in chemical compounds [9]. The media used in the filtration process can be granular sand beds, pebbles, anthracite, glass, small coal particles, or any stable material. The most common filter material is silica sand. The fact that sand is cheap compared to other filter materials, easy to find and effective results have caused it to be widely used. Anthracite or other filter materials are generally used with sand material in the construction of double or multi-layer (multi-media) filter beds that provide higher capacity [10, 11].

Filters consist of three groups as single media, dual media and multi media according to the filter media used. Single media filters are one type of filters and generally the filter media is sand or compressed anthracite. If the size of the filter material in the bed is the same, it is called homogeneous single media filters, if it is different, it is called heterogeneous single media filters. In dual media filters, there are two types of filter material in the filter bed. Multimedia filters contain more than two filter materials [12].

Filters consist of two groups, gravity operated and pressurized, depending on the operating conditions. Gravity operated filters are the process of filtering water from the filter media by gravity effect. Outlet water pressure in these filters is equal to atmospheric pressure. Gravity operated filters are divided into two as slow sand filters and rapid sand filters according to their working speed [13].

Treatment technology with granular activated carbon is the ideal solution for removing chlorinated-hydrocarbons and trihalomethanes, disinfection by-products, volatile organics, pesticides and micro-contaminants that cause taste and odour in drinking water.

Pressure filters are generally made in the form of tanks. The force that moves the water in these filters is the pressure difference at the filter inlet and outlet. The most important properties of these filters is that they do not come into contact with the atmosphere. Pressure filters are made in the form of vertical pressure filters and horizontal pressure filters [13].

### 2.1. Slow sand filtration

In this system, the filter speed changes between 0.1-0.5  $\text{m}^3/\text{m}^2\cdot\text{h}$  In slow sand filters, fine-grained sand material with an effective diameter of 0.15-0.35 mm is used for the filter media. In slow sand filters, the thickness of the

filter media (sand layer) should be between 0.6-1.2 m. Since the grain diameter of the sand is small, suspended and colloid substances in the inlet water cannot arrive at the bed depth of the filter. Therefore, clogging occurs in the upper layer of the filter media [14].

## 2.2. Rapid sand filtration

In rapid sand filters, filter speed is between 5–15 m/s. The grain diameter of the sand to be selected should be between 0.5–2 mm and the bed thickness should be between 0.5–2 m. It should be noted here that the grain size is uniform. Due to the high speed of the filter and the large flow rate passing through the filter area, rapid sand filters clog faster than slow sand filters. Clogged rapid sand filters are cleaned by backwashing. Backwash time is calculated according to the head loss [15].

The backwashing process takes place by reversing the water flow direction. The filter bed expands during backwashing. The pollutants kept in the pores of the particles are cleaned by rubbing them against each other. The important point is to reduce the particle size and increase the densities in order to prevent displacement during backwashing. For example, sand is used as the middle layer, anthracite which is a lighter material on top of it, and magnetite, which is a heavy material at the bottom layer [16].

## 2.3. Granular activated carbon

They filter synthetic and organic chemicals depending on the pollutant type and concentration [17]. Granular activated carbon filters can be used in place of or combined with slow sand filters. Thus, the need for excessive filtration is reduced. Therefore, they are often used in situations where space is a limiting factor [18]. Activated carbons are frequently used as filter media with their high de-chlorination kinetics and hydrocarbon adsorption capacity. Coconut-based activated carbons are generally preferred in drinking water treatment processes, while coal-based activated carbons are preferred in wastewater treatment applications.

## 2.4. Pressurized multi-media filtration

In the multi-layer pressure filtering process, the waste water coming into the system is sprayed to the filtering tank from above through nozzles. As the wastewater moves down through the filter media, it passes through the media of different pore diameters. During this transition, suspended solids and contaminants such as clay and silt that cause turbidity are retained. The treated water passing through the nozzles placed on the bottom of the tank is sent to the storage tank. The pressure of the system increases as contaminants accumulate in the media during filtration. In this case, it is necessary to perform a backwashing process in order to remove the contaminants accumulated between the media. In the backwash process, the flow of water is reversed and the system is supplied with water at high speeds from the bottom. Thus, the particles between the media are cleaned by reverse flow. In the backwash mode, there are enlargements in the media environments. This is an important parameter to be considered in the multi-layer filtering system to be designed [19]. The components of the multimedia system are shown in Figure 1.

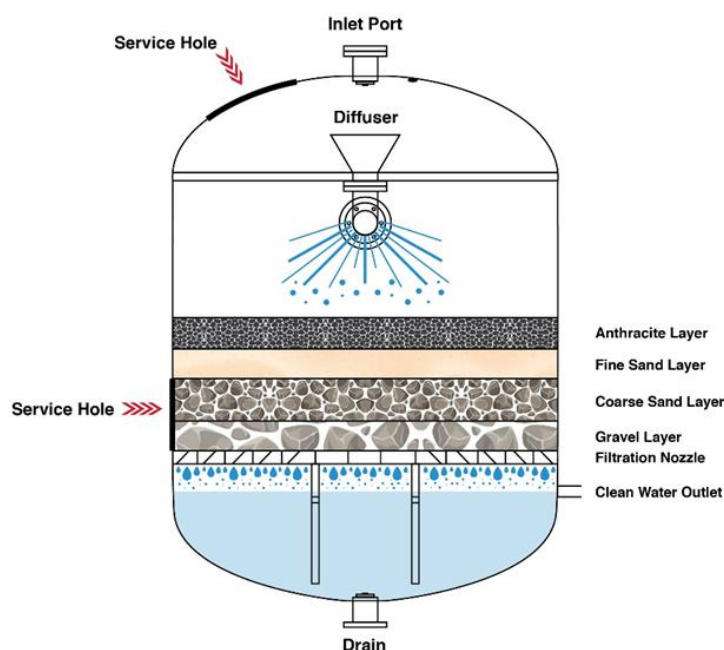


Figure 1. The components of the multimedia system.

### 3. Design parameters of filtration system

Some parameters are determined by engineers in the design of filtration systems. The main design parameters to be determined are the type and physical properties of the filter material, filtration rate control method, pressure losses, and backwashing process.

#### 3.1 Filter materials

Various filtering media can be used in multi-media filtration [20, 21]. Silica sand is most commonly used in the world and in Turkey. A coarser but less dense material (usually anthracite) is placed on silica sand. Anthracite is a natural mineral used as a top layer filtration mineral. The use of multi-layer filter materials has become commonly in developed countries. Media with different characteristics are used according to the diversity of pollutants from water [9].

Quartz sand is used as filtration media or substrate depending on the suspended solid particle size and application. It increases filtration efficiency by reducing retention time and pressure loss with high flow rates. Garnet media is a high-density filter media. It is generally used as base media. Increases productivity with sand, gravel and anthracite. It should have the necessary hardness properties for maximum efficiency and should be rounded rather than angular. Calcite media is a calcium carbonate compound. It is used to neutralize acid. Manganese green sand is a siliceous media treated for the treatment of water containing iron, manganese and hydrogen sulphide. Dolomite is a granular calcium carbonate filtration media with a particle size of 1 to 2 mm. This media is used for adjusting the pH level of drinking water and for the remineralization of desalinated water [22, 23].

#### 3.2 Filtration hydraulics

The law that best explains the flow of fluid in a porous environment is Darcy's Law. According to Darcy's Law, the filter speed ( $V_f$ ) is directly proportional to the permeability coefficient of the filter medium and the hydraulic gradient. Accordingly, the filter speed is expressed by Equation 1 [24].

$$V_f = k \times l \quad (1)$$

Here,  $V_f$  is the filter speed (m/s),  $k$  is the permeability coefficient,  $l$  is the hydraulic slope. Hydraulic slope is the ratio of the distance between the water surfaces to the bed thickness in filters and it is expressed as  $l = H/L$ .  $H$  (m) is the distance between water surfaces, that is, the load container,  $L$  (m) is the thickness of the bed. If this formula is substituted in Equation 1, the expression giving the filtration rate will be as in Equation 2.

$$V_f = k \times \frac{H}{L} \quad (2)$$

Carmen-Kozeny or Sabri Ergün equations are used to calculate head losses of filtration units. The expression that gives the permeability coefficient in a filter bed with a continuous flow of diameter  $d$  according to the Carman-Kozeny equation is given in Equation 3.

$$k = \frac{\rho}{180 \times \vartheta} \times \frac{\varphi^3}{(1-\varphi)^2} \times d^2 \quad (3)$$

Here;  $\rho$  is the density,  $\vartheta$  the kinematic viscosity,  $\varphi$  the porosity and  $d$  (m) the grain diameter. The porosity value varies according to the type of filter material. Kinematic viscosity is a temperature dependent parameter and is calculated using Equation 4.  $T$  refers to temperature in °C.

$$\vartheta = \frac{(1.31) \times 10^{-6}}{(0.72) + (0.028 \times T)} \quad (4)$$

The diameter  $d$  of the filter material is found depending on the shape coefficient  $\theta$  and the specific grain diameter  $d_s$ . Accordingly,  $d$  is calculated using the formula in Equation 5.

$$d = d_s \times \theta \quad (5)$$

The shape coefficient varies according to the shape of the material used in the filter medium. It changes by taking a value of 1 if the material is spherical, 0.7 if the broken material is close to the sphere geometry, 0.95 if it is close to the sphere geometry, and 0.7-0.95 in other shapes [24].

When the value of  $k$  given in Equation 3 is replaced in Equation 2, the load loss is calculated as in Equation 6 according to the Carmen-Kozeny equation. The Carmen - Kozeny equation is often used for laminar flows.

$$H = \frac{V_f \times L}{d^2} \times \frac{1800 \times \vartheta}{\rho} \times \frac{(1-\varphi)^2}{\varphi^3} \quad (6)$$

In addition, the Sabri Ergün equation, which is a broader equation that includes laminar flow, transition region and turbulent flow, is used [24].

$$\frac{H}{L} = \frac{150 \mu}{g \cdot p} \times \frac{(1-\varphi)^2}{\varphi^3} \times (S/6)^2 \times V_f + 1.75 \frac{(1-\varphi) S V_f^2}{\varphi^2 \cdot 6 g} \quad (7)$$

Here:

$H$  = head loss

$L$  = Mattress thickness

$g$  = acceleration of gravity

$\rho$  = density

$\varphi$  = porosity

$S$  = specific surface

$\mu$  = dynamic viscosity

$V_f$  = filter speed

Specific surface  $S$  in Equation 7 refers to the area of grain surface per unit volume. The first term of the Sabri Ergün equation is similar to the Carmen-Kozeny equation. The second part expresses the energy losses [24].

### 3.3 Backwashing

Backwashing is the removal of contaminants accumulated on the material in the filter bed by washing the filter upwards. There should be no material loss during backwashing. In this process, the filter bed is made fluid. When the bed is fluid, the upward force (pressure drop) and the downward force and the weight of the bed under water are equal. This is mathematically represented in Equation 8 [24].

$$\rho \cdot g \cdot Z \cdot A = (1-\varphi) \cdot L \cdot (\rho_s - \rho) \cdot g \cdot A \quad (8)$$

Here:

$\rho$ : density of water (kg/m<sup>3</sup>)

$\rho_s$ : density of the material (kg/m<sup>3</sup>)

$L$ : bed thickness (m)

$\varphi$ : Porosity of the bed

$g$ : acceleration of gravity

$Z$ : head loss in the filter bed during backwashing

$A$ : Filter bed surface area (m<sup>2</sup>)

Another parameter in backwash is the expansion percentage ( $E$ ). This percentage can be calculated using Equation 9.

$$E = 100 \frac{L_e - L}{L} = 100 \frac{\varphi_e - \varphi}{1 - \varphi_e} \quad (9)$$

Here  $L_e$  and  $\varphi_e$  show the expanded bed thickness and porosity, respectively.

The total head loss is calculated using Equation 10.

$$H = H_{base} + H_{bed} + H_{pipe} \quad (10)$$

### 3.4 Physical and chemical parameters

#### 3.4.1 Turbidity (Appearance) and Colour

Drinking and potable water should be clear. Turbidity in water is caused by the presence of silt, clay, degraded organic matter, plankton and bacteria. Turbid water can be pathogenic (may contain disease-causing bacteria).

Pathogenic bacteria can settle in the pores of solid particles that create turbidity. Colour is a very important property for drinking water. Clean waters are colourless. Organic substances are found in yellow or brown waters, and iron and manganese in reddish or dark brown waters. It gives colour to water in substances that are dissolved in water and in colloidal form.

### **3.4.2 Smell and Taste**

Drinking and potable water should be odourless and tasteless. In general, the smell and taste of the waters come from organic substances, living and non-living vegetable organisms (algae), metals (iron, manganese, etc.), phenol, chlorine and chlorine compounds. Humus, acidic, ferrous and manganese waters give the water a taste of ink and sulphurous hydrogen water with a stinky egg smell. Waters with large amounts of chloride will have a salty taste.

### **3.4.2 pH value**

The pH value indicates that the water is acidic or alkaline in character. Pure water has a pH of 7. A low pH value indicates that the water has an acid character and a high pH value indicates a basic character. The pH value is of great importance in cleaning the waters. Treatment of iron, manganese compounds in water, taste, odour and corrosion control are directly related to the pH of the water. The optimum limits of pH, which is an important factor in biological and chemical systems of natural waters, for aquatic life are between 8.5 - 9.0. The high pH value also changes the toxicity of other pollutants.

### **3.4.3 Hardness**

The hardness of the water; It is the property of polyvalent metal ions in water to form insoluble compounds with soaps (organic salts formed by high fatty acids of potassium and sodium). The most important salts that create hardness in water are calcium and magnesium ions. Soap is precipitated especially by calcium and magnesium ions that are always present in water. Water hardness is also used as a contamination indicator.

### **3.4.5 Sulphate**

Sulphate in water resources is generally caused by the soil structure containing sulphate, sulphate fertilizers used in agricultural lands, waste paper, H<sub>2</sub>SO<sub>4</sub>, pharmaceutical industry, sugar factory and dairy industry wastes reaching the receiving water environment. Sulphate is one of the parameters that should be examined especially in terms of aquatic life. Since the sulphate ion is essential for plant nutrition, it should be present in all irrigation water. Sulphated waters cause the destruction of concrete and iron pipes to lose their durability.

### **3.4.6 Chloride**

Chloride, which is present in almost all natural waters, is present in high amounts in waters that are filtered from mineral salt deposits and under the influence of sea water. Because more than half of the dissolved NaCl ion concentration in sea water forms chloride. The amounts of chloride ions are an indicator for healthy water. The amount of chloride in many drinking waters does not exceed 30 mg/lit. This chloride concentration rises in waters close to sea and rock salt deposits. Excessive amount of chloride in water spoils the taste of the water. Therefore, the chloride concentration should not be more than 250 mg/lit. If this amount is exceeded, water becomes undrinkable in terms of taste, even if there is no health hazard.

### **3.4.7 Nitrite**

Source of nitrite in water; organic substances, nitrogenous fertilizers and some minerals in nature do not constitute. Nitrite occurs from the oxidation of nitrogen by means of ammonia. Therefore, the formation of nitrite is a factor that reduces the oxygen in the water. Another negative effect of nitrogen and therefore nitrite is that it causes eutrophication with water due to nitrification. This event is a factor that increases the pollution in the water. The presence of nitrite in water is very important for human and living health. Because; nitrite forms nitrosamines and nitroamides in an acidic environment.

### **3.4.8 Nitrate**

Nitrate is one of the important water quality parameters that affect efficiency in water. Nitrate ions in water are caused by the oxidation of ammonia resulting from protein decomposition of animal and vegetable wastes, nitrate fertilizers used in agricultural fields, direct oxidation of nitrogen-to-nitrogen oxides as a result of electrical

discharges in the atmosphere and the reactions of these oxides in water. The amount of nitrate in water varies widely in nature. The amount of precipitation may increase significantly after the dry periods. While the amount of chlorinated water is low, the amount of chlorine increases in non-chlorinated water. Nitrates can also be an indicator of water pollution.

### **3.4.9 Ammonia**

Ammonia concentrations in drinking water are indicative of organic contamination. The toxic effect of ammonia on living beings increases with the lack of oxygen, increase in temperature and the presence of other toxic substances. It is known that some of the nitrogen combined with the organics in the clay and soil is converted into ammonia by the bacteria in the soil. The level of this transformation is; Although it varies depending on the soil type, climate and the type of plant grown at that soil level, it is at most 3%.

## **4. Results**

The factors to be considered in order to obtain an effective result in the selection of the filtration system can be listed as follows.

- Maximum flow rate required
- System operating temperature
- Flow
- Nature of suspended solids or turbidity
- Water analysis of feed water
- Quality of the water to be treated
- Availability of sufficient water source for backwashing

The filter base should be made in a way that it does not clog and prevents the material in the filter bed from mixing with the filtered water. There is a sand and gravel layer under the filter bed at the filter base, and nozzles and manifold under it. The sand-gravel layer under the filter bed must be arranged very well. There is a fine-grained layer at the top of this layer.

The biggest head loss in filters depends on filter bed thickness and material density. Taking this issue into consideration in filtration designs, large bed thickness is preferred in order to keep the filtration time long.

Sometimes water and sometimes air are used in backwashing processes. In systems where water is used, backwash rate changes between 37-70 m<sup>3</sup>/m<sup>2</sup>.h, while compressed air velocity varies between 1-1.5 m<sup>3</sup>/m<sup>2</sup>.min.

Fast sand filters require low construction costs and high operating costs. These filters should be cleaned within 1-3 days.

For slow sand filters, there are high construction costs and low operating costs. These systems should be cleaned after 90-120 days.

## **5. Discussion**

Sand Filtration Systems is a technology recommended by the World Health Organization as a wastewater treatment technique. Large-scale technologies such as nano filtration, reverse osmosis, ultraviolet filtration, membrane bioreactors are available, but they are not cost effective. Sand Filtration Systems are more cost-effective systems where raw materials can be obtained in cheap ways. They are used to treat all types of waste, drinking or rainwater. The basic mechanism of this system lies primarily in the development of media mediums responsible for the removal of bacteria and viruses.

Hydrophobic interactions, hydration and Van der Waals forces, surface roughness and bridging at the macromolecular level are mechanical factors responsible for bacterial adhesion and make their removal from water difficult [25].

Studies have shown that aluminium hydroxide or iron oxide coated sand gives more effective results than uncoated sand [26]. However, whether placing it on the sand or at another depth will yield the same results is an important research that needs to be done yet.

In the future, the focus should be on researching the effects of metal coating of filtering sands on productivity and human health.

## **6. Conclusion**

Parameters such as flow rate, filter size, contaminant rate and types in water, filter depth, head loss change the design of filtration systems significantly. The proposed in this study can be used to optimize the design of sand

filtration systems. Alternatives can be designed with media of different specific gravities and sizes. The results obtained by examining various facility designs are as follows.

- Methods developed for single media can also be used for multimedia filters.
- Polyacrylamides, suspended solids, sulphate, nitrite, water hardness, ammonium greatly alter the performance of all filtration systems and must be considered in filter design.
- Filter design should not be limited to general standards. It should be designed according to the source of the water. The operating results of many facilities have shown that the specific design is suitable for specific situations.

## Funding

This research received no external funding.

## Author contributions

**Ece Kalay:** Conceptualization, Methodology, Software **Hasan Sarıoğlu:** Data curation, Writing-Original draft preparation, Software, Validation. **İskender Özkul:** Visualization, Investigation, Writing-Reviewing and Editing.

## Conflicts of interest

The authors declare no conflicts of interest.

## References

1. Pintilie, L., Torres, C. M., Teodosiu, C., & Castells, F. (2016). Urban wastewater reclamation for industrial reuse: An LCA case study. *139*, 1-14.
2. Başkan, T. (2006). *Aritılmış Evsel Atıksuların Tarımda Sulama Amaçlı Yeniden Kullanılması*. (Yüksek Lisans), İstanbul Teknik Üniversitesi,
3. Asan, C. (2013). *Gri suların yeniden kullanımında membran biyoreaktör (MBR) uygulamaları*. (Yüksek Lisans Tezi), Ondokuz Mayıs Üniversitesi,
4. Büyükkamacı, N. (2009). *Su yönetiminin etkin bileşeni: yeniden kullanım*. Paper presented at the İzmir Kent Sorunları Sempozyumu.
5. Oron, G., Gillerman, L., Buriakovsky, N., Bick, A., Gargir, M., Dolan, Y., . . . Hagin, J. J. D. (2008). Membrane technology for advanced wastewater reclamation for sustainable agriculture production. *218*(1-3), 170-180.
6. Yim, S.-K., Ahn, W.-Y., Kim, G.-T., Koh, G.-W., Cho, J., & Kim, S.-H. J. D. (2007). Pilot-scale evaluation of an integrated membrane system for domestic wastewater reuse on islands. *208*(1-3), 113-124
7. Hyun, K.-S., Lee, S.-J. J. W. S., & Technology. (2009). Biofilm/membrane filtration for reclamation and reuse of rural wastewaters. *59*(11), 2145-2152.
8. Nakada, N., Shinohara, H., Murata, A., Kiri, K., Managaki, S., Sato, N., & Takada, H. J. W. r. (2007). Removal of selected pharmaceuticals and personal care products (PPCPs) and endocrine-disrupting chemicals (EDCs) during sand filtration and ozonation at a municipal sewage treatment plant. *41*(19), 4373-4382.
9. Muhammad, N., Parr, J., Smith, M. D., & Wheatley, A. D. (1997). Removal of heavy metals by slow sand filtration.
10. Bruni, M., & Spuhler, D. J. S. i. (2012). Slow Sand Filtration.
11. Bland, L. (2008). Final Report: Sustainable Community Development–Water Slow-Sand Filtration. US EPA Grant Number SU833544. In.
12. D'Alessio, M., Yoneyama, B., Kirs, M., Kisand, V., & Ray, C. J. S. o. t. T. E. (2015). Pharmaceutically active compounds: Their removal during slow sand filtration and their impact on slow sand filtration bacterial removal. *524*, 124-135.
13. Sánchez, L., Marin, L., Visscher, J., Rietveld, L. J. D. W. E., & Science. (2012). Low-cost multi-stage filtration enhanced by coagulation-flocculation in upflow gravel filtration. *5*(1), 73-85.
14. Khengaoui, K., Mahammed, M. H., Touil, Y., & Amrane, A. J. E. P. (2015). Influence of secondary salinity wastewater on the efficiency of biological treatment of sand filter. *74*, 398-403.
15. Vries, D., Bertelkamp, C., Kegel, F. S., Hofs, B., Dusseldorp, J., Bruins, J., . . . Van den Akker, B. J. W. R. (2017). Iron and manganese removal: Recent advances in modelling treatment efficiency by rapid sand filtration. *109*, 35-45.
16. Han, S., Fitzpatrick, C. S., & Wetherill, A. J. W. r. (2009). The impact of flow surges on rapid gravity filtration. *43*(5), 1171-1178.
17. Arena, N., Lee, J., & Clift, R. J. J. o. C. P. (2016). Life Cycle Assessment of activated carbon production from coconut shells. *125*, 68-77.

18. McCleaf, P., Englund, S., Östlund, A., Lindegren, K., Wiberg, K., & Ahrens, L. J. W. r. (2017). Removal efficiency of multiple poly-and perfluoroalkyl substances (PFASs) in drinking water using granular activated carbon (GAC) and anion exchange (AE) column tests. *120*, 77-87.
19. Smith, K., Li, Z., Chen, B., Liang, H., Zhang, X., Xu, R., . . . Liu, S. J. C. (2017). Comparison of sand-based water filters for point-of-use arsenic removal in China. *168*, 155-162.
20. Soyer, E., Akgiray, Ö., Eldem, N. Ö., & Saatçı, A. M. J. C. S., *Air, Water*. (2010). Crushed recycled glass as a filter medium and comparison with silica sand. *38*(10), 927-935.
21. Evans, G., Dennis, P., Cousins, M., Campbell, R. J. W. S., & supply, t. W. (2002). Use of recycled crushed glass as a filtration medium in municipal potable water treatment plants. *2*(5-6), 9-16.
22. Rutledge, S. O., Fahie, C., & Gagnon, G. A. (2002). Assessment of crushed-recycled glass as filter media for drinking water treatment.
23. WATER, A. H. O. D. (2010). *Water quality and treatment*.
24. Eroğlu, V. J. İ. T. Ü. K. (1991). *Su Tasfiyesi* (3. Baskı). (1439), 175-248.
25. Kim, S.-B., Park, S.-J., Lee, C.-G., Choi, N.-C., Kim, D.-J. J. C., & Biointerfaces, S. B. (2008). Bacteria transport through goethite-coated sand: Effects of solution pH and coated sand content. *63*(2), 236-242.
26. Scholl, M. A., Harvey, R. W. J. E. S., & Technology. (1992). Laboratory investigations on the role of sediment surface and groundwater chemistry in transport of bacteria through a contaminated sandy aquifer. *26*(7), 1410-1417.



© Author(s) 2021. This work is distributed under <https://creativecommons.org/licenses/by-sa/4.0/>